



1 **Leeuwin Current dynamics over the last 60 kyrs – relation**
2 **to Australian extinction and Southern Ocean change**

3 Dirk Nürnberg¹, Akintunde Kayode¹, Karl J.F. Meier², Cyrus Karas³

4 ¹GEOMAR Helmholtz Centre for Ocean Research Kiel, Wischhofstr. 1-3, D-24148 Kiel, Germany

5 ²Institute of Earth Science, Heidelberg University, Im Neuenheimer Feld 234, Heidelberg D-69120, Germany

6 ³Universidad de Santiago de Chile, Av. Bernardo O'Higgins 3363, Santiago, Chile

7 *Correspondence to:* Dirk Nürnberg (dnuernberg@geomar.de)

8

9 *Keywords:* Leeuwin Current, Abrupt Climate Change, Southern Ocean, ENSO, Australian extinction, Australian
10 biomass burning, human colonization

11



12 **Abstract**

13 The Leeuwin Current flowing southward along West Australia is an important conduit for the
14 poleward heat transport and interocean water exchange between the tropical and the
15 subantarctic ocean areas. Its past development, and its relationship to Southern Ocean change
16 and to Australian ecosystem response, however is largely unknown. We here reconstruct sea
17 surface and thermocline temperatures and salinities from foraminiferal-based Mg/Ca and stable
18 oxygen isotopes from offshore southwest and southeast Australia reflecting the Leeuwin
19 Current dynamics over the last 60 kyrs. Its variability resembles the biomass burning
20 development in Australasia from ~60-20 ka BP implying that climate-modulated changes
21 related to the Leeuwin Current most likely affected Australian vegetational and fire regimes.
22 In particular during ~60-43 ka BP, warmest thermocline temperatures point to a strongly
23 developed Leeuwin Current during Antarctic cool periods when the Antarctic Circumpolar
24 Current weakened. The pronounced centennial-scale variations in Leeuwin Current strength
25 appear in line with the migrations of the Southern Hemisphere frontal system and are captured
26 by prominent changes in the Australian megafauna biomass. We argue that the concerted action
27 of a rapidly changing Leeuwin Current, the ecosystem response in Australia, and human
28 interference since ~50 BP enhanced the ecological stress on the Australian megafauna until a
29 tipping point was reached at ~43 ka BP, after which faunal recuperation no longer took place.
30 While being weakest during the last glacial maximum, the deglacial Leeuwin Current
31 intensified at times of poleward migrations of the Subtropical Front. During the Holocene, the
32 thermocline off South Australia was considerably shallower compared to the short-term glacial
33 and deglacial periods of Leeuwin Current intensification.

34

35

36

37



38 **1 Introduction**

39 The southern margin of Australia is one of the world's largest latitude-parallel shelf and slope
40 regions (James et al., 1994), affected by large boundary currents to the east (East Australian
41 Current) and west (Leeuwin Current), which transport tropical ocean heat southward (e.g.
42 Wijeratne et al., 2018). Many studies highlighted the seasonal and interannual variability
43 associated with these currents, but also the impact of the decadal ENSO climate variability on
44 the strength and transport variability of these currents (e.g., Feng et al., 2003; Holbrook et al.,
45 2011; Wijeratne et al., 2018).

46 The warm and saline Leeuwin Current, an eastern boundary current that flows southward along
47 West Australia, originates from the Indonesian-Australian Basin and is fed by Indonesian
48 Throughflow waters (ITW) and the eastward-directed Eastern Gyral Current (Meyers et al.,
49 1995; Domingues et al., 2007) (Fig. 1). The Leeuwin Current turns east into the Great
50 Australian Bight (Cresswell and Golding, 1980; Church et al., 1989; Smith et al., 1991) and
51 shapes the temperature and salinity conditions, as well as water column stratification off
52 western and southern Australia (Legeckis and Cresswell, 1981; Herzfeld and Tomczak, 1997;
53 Li et al., 1999; Middleton and Bye, 2007; Holbrook et al., 2012). Wells and Wells (1994)
54 concluded from micropaleontological studies that the Leeuwin Current likely stopped flowing
55 during glacial periods, while the northwest-directed West Australian Current gained strength,
56 resulting in a large-scale reorganization of the regional circulation patterns. Martinez et al.
57 (1999) reported on the reduced occurrence of tropical planktonic species in the eastern Indian
58 Ocean during glacial periods, while abundances of intermediate and deep-dwelling species
59 increased, which they related to a weakened Leeuwin Current. Spooner et al. (2011) argued
60 instead, that the Leeuwin Current remained active although weakened during the last five
61 glacial periods, while the West Australian Current strengthened.

62 For the interglacial Marine Isotope Stage (MIS) 5, 7 and 11, Spooner et al. (2011) inferred a
63 stronger Leeuwin Current due to an enhanced ITF contribution. De Deckker et al. (2012) and
64 Perner et al. (2018) attributed the alternating warm and cold phases in the Great Australian
65 Bight to changes in both Leeuwin Current-related heat export from the Indo-Pacific Warm Pool
66 and latitudinal shifts of the Subtropical Front (STF). A study from off Tasmania (Nürnberg et
67 al., 2004) already pointed to a STF, which was commonly located further to the south during
68 interglacials, while its glacial position moved northward and allowed subantarctic waters to
69 expand northward. Moros et al. (2009) suggested that the STF was located closer to the
70 southern Australian coast during the early Holocene (~10-7.5 ka BP) than its current position
71 today at ~45°S in winter.



72 Despite the many efforts to understand the paleoceanographic setting south of Australia (e.g.,
73 Wells and Wells, 1994; Findlay and Flores, 2000; Barrows and Juggins, 2005; Nürnberg and
74 Groneveld, 2006; Calvo et al., 2007; Moros et al., 2009; Spooner et al., 2011; De Deckker et
75 al., 2012; Lopes dos Santos, 2012; Perner et al., 2018), no proxy studies but only few modelling
76 studies concentrate on the subsurface development (e.g., Schodlok and Tomczak, 1997;
77 Middleton and Cirano, 2002; Middleton and Platov, 2003; Cirano and Middleton, 2004;
78 Middleton and Bye, 2007; Pattiaratchi and Woo, 2009). The aim of our study is to fill this
79 important gap and to reveal changes in the Leeuwin Current over the last 60 kyrs. Stable oxygen
80 isotope ($\delta^{18}\text{O}$) and Mg/Ca-based reconstructions of surface and thermocline temperatures
81 ($\text{SST}_{\text{Mg/Ca}}$; $\text{TT}_{\text{Mg/Ca}}$) and $\delta^{18}\text{O}_{\text{sw-ivc}}$ (approximating surface and thermocline salinity) from two
82 sediment cores off southern Australia (MD03-2614 and MD03-2609) allow to address the past
83 dynamics of the vertical water column structure south of Australia in response to latitudinal
84 shifts of oceanographic and atmospheric frontal systems, and the impact of the Southern Ocean
85 change in the study area.

86

87 **2 Modern oceanographic setting**

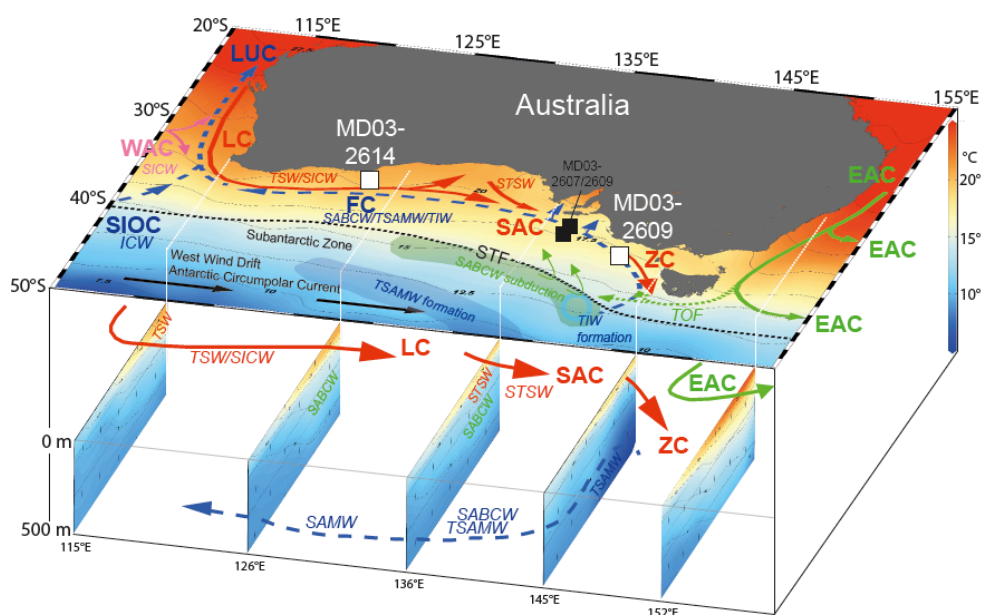
88 **2.1 Currents**

89 The Leeuwin Current and the Flinders Current are the two current systems mainly affecting
90 the ocean region south of Australia (Fig. 1). The Leeuwin Current flows southwards along the
91 western Australia shelf break and is characterized as shallow (upper ~200 m) coastal current,
92 with low-salinity and nutrient-depleted waters that originate from the Indo-Pacific Warm Pool.
93 After passing Cape Leeuwin, it turns east into the Great Australian Bight as far as ~124°E
94 (Ridgway and Condie, 2004). The Leeuwin Current's tropical water characteristics gradually
95 alter, becoming saltier, cooler, and denser as it flows east due to air-sea interactions, subtropical
96 addition, and eddy mixing with Indian Ocean and Southern Ocean waters (c.f. Richardson et
97 al., 2019). Seasonal variations in the Leeuwin Current strength (Ridgway and Condie, 2004;
98 Cirano and Middleton, 2004) reveal that the Leeuwin Current is strongest near the shelf-edge
99 in austral winter (June–July) with a maximum poleward geostrophic transport of ~5 Sv (10^6
100 $\text{m}^3 \text{s}^{-1}$), and weakest in austral summer with a mean transport of ~2 Sv (Holloway and Nye,
101 1985; Rochford, 1986; Feng et al., 2003; Ridgway and Condie, 2004).

102 Although relying on different forcing mechanisms, the South Australian Current is widely
103 regarded as the extension of the Leeuwin Current and develops in the east of the Great
104 Australian Bight. In the Bass Strait, the Leeuwin Current / South Australian Current-system
105 continues south as Zeehan Current (Ridgway and Condie, 2004; Richardson et al., 2018). South



106 of Australia, the Leeuwin Current System meets the northern boundary of the eastward flowing
107 Antarctic Circumpolar Current (ACC). Below, the deeper (300-400 m), equatorward flow of
108 the Leeuwin Undercurrent is noted (Spooner et al., 2011). During austral summer times, when
109 the Leeuwin Current is weak, the equatorward Capes Current establishes at the inner shelf
110 around Cape Leeuwin. Its formation is related to regional upwelling, bringing water masses
111 from the Flinders Current and the lower layers of the Leeuwin Current towards the upper shelf
112 areas (cf. McClatchie et al., 2006).



113
114 **Figure 1.** Top: Regional surface and subsurface circulation pattern off S Australia underlain by the modern annual
115 SST pattern (using Ocean Data View v. 5.1.7; Schlitzer, 2019; World Ocean Atlas, WOA 2013). Sediment core
116 locations (MD03-2614 and -2609) studied here are marked by white squares. Black squares = reference sites.
117 Surface currents in red and green: LC = Leeuwin Current; WAC = West Australian Current; SIOC = South Indian
118 Ocean Current; SAC = South Australian Current; ZC = Zeehan Current; EAC = East Australian Current; TOF =
119 Tasman Outflow. Subsurface currents in blue: FC = Flinders Current; LUC = Leeuwin Undercurrent. Water
120 masses transported by currents: TSW = Tropical Surface Water; ICW - Indian Central Water; SICW = South
121 Indian Central Water; STSW = Subtropical Surface Water; SABCW = South Australian Basin Central Water;
122 SAMW = Subantarctic Mode Water; TSAMW = Tasmanian Subantarctic Mode Water; TIW = Tasmanian
123 Intermediate Water. Sites of SABCW, TIW and TSAMW formation are indicated. STF = Subtropical Front
124 (dashed black line). Bottom: N-S-oriented temperature profiles (February) of the upper 500 m (dotted white lines;
125 using Ocean Data View v. 5.1.7; Schlitzer, 2019). Currents, water masses and sites of mode and intermediate
126 water formation from Richardson et al. (2019).



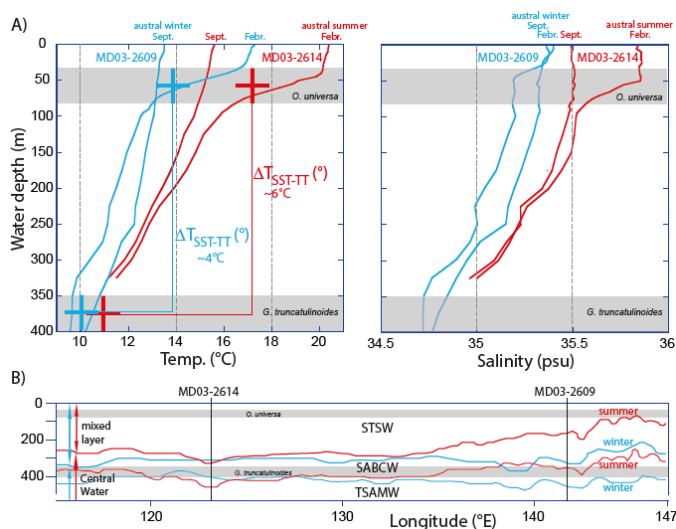
127 The westward-directed Flinders Current is a subsurface northern boundary current along the
128 continental slope of south Australia (Middleton and Cirano, 2002; Cirano and Middleton, 2004)
129 (Fig. 1). Maximum transport is at ~400-800 m, with velocities of up to 8 cm s^{-1} (Middleton and
130 Bye, 2007). It originates within the Subantarctic Zone and carries Subantarctic Mode Water
131 (SAMW) and Antarctic Intermediate Water (AAIW) across the STF (McCartney and Donohue,
132 2007). Southeast of Australia, the Flinders Current is fed and strengthened by the Tasman
133 Outflow, a remnant of the East Australian Current, which injects Pacific waters into the South
134 Australian Basin (Rintoul and Sokolov, 2001) and becomes an important component of the
135 westward flow south of Australia (Speich et al., 2002). The Flinders Current fluctuates in
136 strength on a seasonal time scale (Richardson et al., 2019), with almost doubled transport (~17
137 Sv) during austral summer compared to winter (~8 Sv).

138 The Leeuwin Undercurrent, which is beneath the Leeuwin Current at depths of ~250-600 m,
139 transports ~5 Sv of saline ($> 35.8 \text{ psu}$), oxygen-rich and nutrient-depleted waters northward as
140 an extension of the Flinders Current (Fig. 1; Thompson, 1984; Smith et al., 1991; Cirano and
141 Middleton; 2004). Both currents are associated with SAMW (Pattiaratchi and Woo, 2009).

142

143 **2.2 Water masses and oceanographic fronts**

144 In this study, we address three water masses within the uppermost 600 m along the continental
145 slope of southern Australia (Fig. 2): Subtropical Surface Water (STSW), South Australian
146 Basin Central Water (SABCW), and SAMW. The subtropical warm and saline STSW
147 originates within the surface mixed layer (upper ~200 m) along Australia's southern margin
148 between 34°S and 38°S as a result of surface heating and enhanced evaporation (James and
149 Bone, 2011) (Fig. 2). STSW constitutes the shallowest water mass along the southern
150 Australian margin and is defined by temperatures $>12^{\circ}\text{C}$ and salinities >35.1 (Richardson et
151 al., 2018). The dissolved oxygen concentration is high (225-250 $\mu\text{mol/L}$), and nutrients are low
152 (Richardson et al., 2018). The water mass is additionally fed by low salinity Tropical Surface
153 Water (TSW) and high salinity South Indian Central Water (SICW) transported by the Leeuwin
154 Current (Cresswell and Peterson, 1993). The maximum depth of the STSW (~100-300 m) is
155 seasonally dependent, being deeper during winter than in summer (Richardson et al., 2018). In
156 winter, the STSW is transported further to the east by the Zeehan Current and may reach the
157 southern tip of Tasmania. During summer, the STSW remains west of $\sim 140^{\circ}\text{E}$ (Newell, 1961;
158 Vaux and Olsen, 1961; Ridgway, 2007; Richardson et al., 2018).



159

160 **Figure 2. Upper ocean hydrological setting south of Australia:** A) Temperature (left) and salinity (right)
161 distribution of the upper 400 m at the western core 2614 location (red) and at the eastern core 2609 location (blue)
162 (c.f. Fig. 1). Only maximum (February; austral summer) and minimum (September; austral winter/spring)
163 temperatures and salinities are indicated. Presumed calcification depths of foraminiferal species analyzed are
164 indicated by gray shadings: *O. universa* at ~50-100 m water depth (Anand et al., 2003; Farmer et al., 2007);
165 *G. truncatulinoides* at ~350-400 m water depth (Cléroux et al., 2008; Anand et al., 2003). Modern average
166 temperatures (crosses) and temperatures gradients between surface and thermocline are indicated for the
167 respective study areas. Data from Ocean Data View v. 5.1.7 (ODV Station labels 12796 and 11161; Schlitzer,
168 2019; WOA; Locarnini et al., 2018). B) Average summer (red) and winter (blue) boundaries between the surface
169 mixed layer (consisting predominantly of STSW) and the Central Water (composed of SABCW and TSAMW),
170 taken from Richardson et al., 2019). Core locations (black vertical lines) and assumed calcification depths of
171 foraminiferal species studied are indicated.

172

173 The SABCW showing a small range in potential density ($26.65\text{-}26.8\text{ kg/m}^3$) is below the
174 surface mixed layer (Fig. 2 B). SABCW is defined by temperatures and salinities of $10\text{-}12^\circ\text{C}$
175 and $34.8\text{-}35.1$, with a weak dissolved oxygen maximum ($> 250\text{ }\mu\text{mol/L}$) (Tomczak et al., 2004;
176 Richardson et al., 2018). Towards the east, the thickness of the SABCW is ~ 200 m, while it
177 decreases to ~ 100 m in the west (Richardson et al., 2018). The thinning of SABCW towards
178 the west is likely attributed to the presence of near-surface subtropical water in the west
179 (STSW), contributed by the strong eastward flowing Leeuwin Current. SABCW likely forms
180 south of the STF between $44\text{-}46^\circ\text{S}$ and $140\text{-}145^\circ\text{E}$ in winter by convective overturning and
181 subduction of the deep mixed layer (Richardson et al., 2018). The subducted SABCW reaches
182 slope depths of $\sim 300\text{-}500$ m at 142°E and $\sim 300\text{-}400$ m at 130°E to 121°E . It is transported



183 eastwards towards Tasmania along the STF by zonal flow. The Flinders Current inflow from
184 the south-eastern margin then carries SABCW north and west along Australia's southern
185 margin, augmented by the Tasman Outflow and equatorward Sverdrup transport (Schodlok and
186 Tomczak, 1997).

187 The coldest and densest SAMW of the Indian Ocean forms by air-sea interaction and deep
188 winter mixing south of Australia between 40°S and 50°S (Wyrki, 1973; McCartney, 1977;
189 Thompson and Edwards, 1981; Karstensen and Quadfasel, 2002; Barker, 2004). SAMW is
190 subducted, thereby ventilating the lower thermocline of the southern hemisphere subtropical
191 gyres (McCartney et al., 1977; Sprintall and Tomczak, 1993). The high-nutrient SAMW is
192 defined as a layer of relatively constant density (pycnostad) along the southern Australian
193 continental slope (Richardson et al., 2019) (Fig. 2). The pycnostad is clearly defined in the east,
194 notably in summer, but diminishes towards the west (Richardson et al., 2018). The SAMW in
195 this region is located at ~400-650 m, with temperatures of ~8-10°C and salinities of 34.6-34.8
196 (Woo and Pattiaratchi, 2008; Pattiaratchi and Woo, 2009), being therefore fresher than the
197 overlying SABCW and STSW. The top SAMW depth varies seasonally from west to east, as
198 it shallows to ~350 m during summer and deepens to ~500 m in winter (Rintoul and Bullister,
199 1999; Rintoul and England, 2002). In particular, the Tasmanian SAMW (TSAMW) is formed
200 in a clearly-defined area at 140-145°E and 45-50°S (Barker, 2004).

201

202 **3 Material and methods**

203 In the framework of the International Marine Global Change Study (IMAGES), Calypso giant
204 piston cores MD03-2614G (termed western core 2614; 34°43.73'S 123°25.70'E; 1070 m water
205 depth; 8.4 m core recovery) and MD03-2609 (termed eastern core 2609; 39°24.17'S
206 141°58.12'E; 2056 m water depth; 24.18 m core recovery) were recovered south of Australia
207 ~100 km south of Cape Pasley and ~250 km northwest of King Island, respectively, during the
208 AUSCAN-campaign with RV Marion Dufresne (MD131) in 2003 (Michel et al., 2003;
209 <https://doi.org/10.17600/3200090>). The chronostratigraphy of core 2614 was published by van
210 der Kaars et al. (2017) and is repeated here, as core 2614 served as reference for the
211 establishment of the core 2609 chronostratigraphy. The age model of core 2609 was established
212 in the framework of this study.

213

214 **3.1 Foraminiferal species selection**

215 The chronostratigraphy and the paleo-reconstructions were established from isotope-
216 geochemical parameters measured within the calcitic tests of the subtropical shallow-dwelling



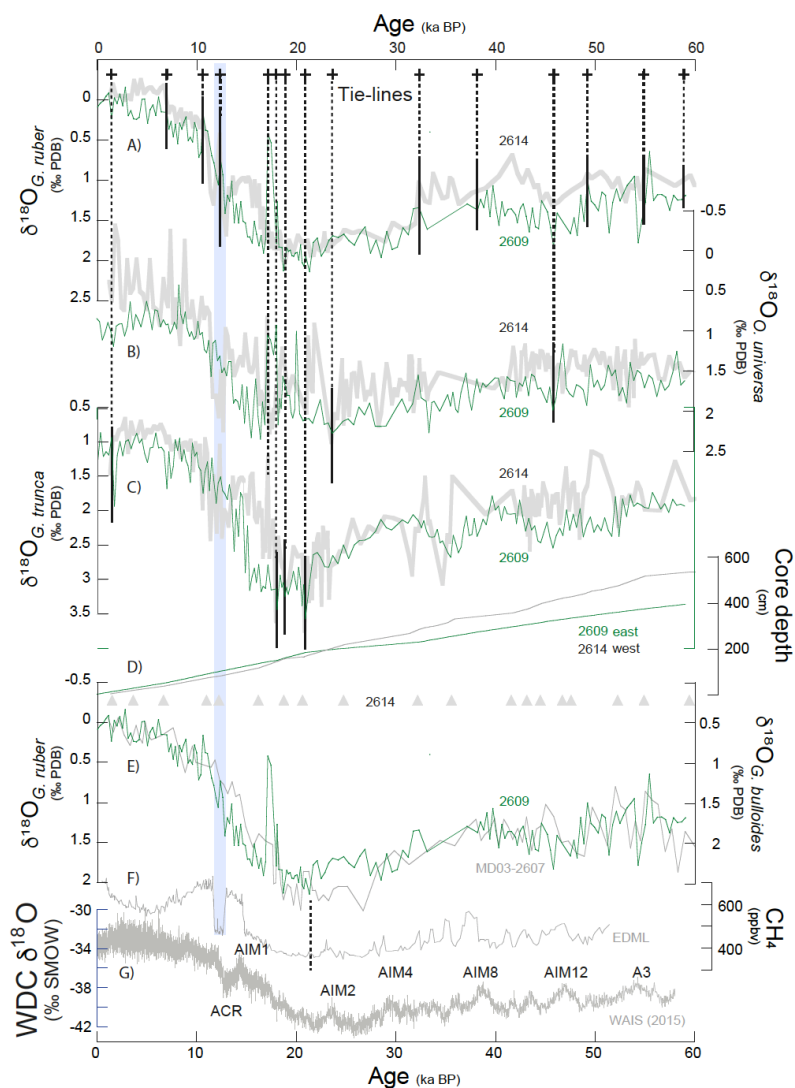
217 planktonic foraminiferal species *Orbulina universa* (d'Orbigny, 1839) (Bé and Tolderlund,
218 1971) and *Globigerinoides ruber*, and the deep-dwelling species *Globorotalia truncatulinoides*
219 (d'Orbigny, 1839) (Lohmann and Schweitzer, 1990). As *O. universa* preferentially lives in the
220 surface mixed layer and the shallow thermocline, we assigned a calcification depth of ~30-80
221 m (c.f. Supplement). The surface-dwelling *G. ruber* is the most representative species of warm
222 and annual surface (<50 m) ocean conditions (Anand et al., 2003; Tedesco and Thunell, 2003).
223 For *G. truncatulinoides* we assume a calcification depth of ~350-400 m (c.f. Supplement),
224 which corresponds to the base of the summer thermocline (Fig. 2; Locarnini et al., 2018). Most
225 of the *G. truncatulinoides* specimens in our samples were encrusted (c.f. Supplement).
226 On average, 10-12 and 30-40 visually clean specimens of *O. universa/G. ruber* and
227 *G. truncatulinoides*, respectively, were hand-picked under a binocular microscope from the
228 narrow >315-400 μm size fraction in order to avoid size-related effects on either Mg/Ca or
229 stable isotopes. *G. truncatulinoides* has no size effect on Mg/Ca (Friedrich et al., 2012), and
230 also $\delta^{13}\text{C}$ and $\delta^{18}\text{O}$ show no systematic changes in the selected size fraction (Elderfield et al.,
231 2002). The foraminiferal tests were gently crushed between cleaned glass plates to open the
232 test chambers for efficient cleaning. Over-crushing was avoided to prevent an excessive sample
233 loss during cleaning procedure. The fragments of the tests were homogenized and split into
234 subsamples for stable isotope (one third) and trace metal analyses (two thirds) and transferred
235 into cleaned vials. Chamber fillings (e.g. pyrite, clay) and other contaminant phases (e.g.
236 conglomerates of metal oxides) were thoroughly removed before chemical cleaning and
237 analyses.

238

239 3.2 Chronostratigraphy

240 3.2.1 Western core 2614

241 The age model of the western core 2614 (Cape Pasley) is based on the linear interpolation
242 between 11 Accelerator Mass Spectrometry (AMS) radiocarbon (^{14}C) dates (van der Kaars et
243 al., 2017; Fig. 3). The well-constrained age model indicates that core 2614 provides a
244 continuous record over the last ~60 kyr (Fig. 3). In addition to the $\delta^{18}\text{O}$ record of *G. ruber* (van
245 der Kaars et al., 2017), we produced $\delta^{18}\text{O}$ records of *O. universa*, and *G. truncatulinoides*.
246 Interesting to note is that a significant and rapid transition to heavy $\delta^{18}\text{O}$ -values in (only)
247 *O. universa* from core 2614 is synchronous to a major atmospheric methane (CH_4) anomaly
248 detected in the Antarctic EDML ice core record (EPICA 2006), further supporting the validity
249 of the initial core 2614 age model (Fig. 3).



250

251 **Figure 3. Chronostratigraphy of the eastern core 2609 (King Island).** The age model is based on the tuning
252 of various planktonic $\delta^{18}\text{O}$ records (A) *G. ruber*, B) *O. universa*, and C) *G. truncatulinoides*; all in green thin
253 lines) to similar records (thick gray lines) of the well-dated reference core 2614 (van der Kaars et al., 2017). In
254 total, 14 tuning tie-lines (stippled lines; solid for the species-specific correlations) were set in order to achieve an
255 optimal fit of the core 2609 and core 2614 $\delta^{18}\text{O}$ records (mean $r^2 = 0.86$). D) Sedimentations rates (green = core
256 2609; gray = core 2614). Gray triangles = age control points established for core 2614 by van der Kaars et al.
257 (2017). E) The age model for core 2609 is supported by the match of its $\delta^{18}\text{O}_{G.ruber}$ record (green) to the adjacent
258 core MD03-2607 $\delta^{18}\text{O}_{G.bulloides}$ record (gray; Lopes dos Santos et al., 2013). F) Atmospheric CH_4 record from
259 EPICA ice core (EPICA, 2006). Blue shading denotes prominent atmospheric CH_4 anomaly synchronous to a
260 distinct reflection in the core 2614 $\delta^{18}\text{O}_{O.universa}$ record. G) West Antarctic Ice Sheet Divide Core $\delta^{18}\text{O}$ record
261 (WAIS Divide Project Members, 2015) as reference for the southern hemisphere climate signal.



262 3.2.2 Eastern core 2609

263 The age model of the eastern core 2609 is based on the tuning of multiple planktonic $\delta^{18}\text{O}$
264 records to those of the well-dated reference core 2614 (van der Kaars et al., 2017) using the
265 software AnalySeries. For both cores, we produced $\delta^{18}\text{O}$ records on *G. ruber*, *O. universa*, and
266 *G. truncatulinoides*, all of which have either different spatial resolutions or even gaps (due to
267 missing species), which are covered by the one or other species (Fig. 3; www.pangaea.de). In
268 a first step, we graphically tuned the $\delta^{18}\text{O}_{G.ruber}$ record of the eastern core 2609 to that of the
269 western core 2614 (van der Kaars et al., 2017), thereby generating 8 tuning tie-lines (Fig. 3A).
270 This correlation was improved in a second step by tying the $\delta^{18}\text{O}_{O.universa}$ records of both cores
271 to each other using 2 additional tie-lines (Fig. 3B). In a last step, we correlated the
272 $\delta^{18}\text{O}_{G.truncatulinoides}$ records of both cores fixing them with 4 additional tie-lines (Fig. 3C).
273 Overall, we achieved an optimized fit of the core 2609 $\delta^{18}\text{O}$ records to the core 2614G reference
274 record (linear correlation = 0.86, averaged from all $\delta^{18}\text{O}$ records), by applying 14 tuning tie-
275 lines. The resulting age-depth relationship of core 2609 is rather smooth, with a subtle change
276 in sedimentation rates at 200-230 cm core depth. The age model implies that the uppermost ~4
277 m of core 2609 capture the last 60 kyrs of environmental change (Fig. 3).

278 Our stratigraphical approach for core 2609 is convincingly supported by the match of the
279 $\delta^{18}\text{O}_{G.ruber}$ record to the $\delta^{18}\text{O}_{G.bulloides}$ record of adjacent core MD03-2607 from Murray Canyon
280 $36^{\circ}57.54'S$ $137^{\circ}24.39'E$, 865 m water depth (Lopes dos Santos et al., 2013; Fig. 3E). The
281 sedimentation rates in both cores 2609 and 2614 vary from 5-20 cm/kyr over the last 60 kyrs
282 (Fig. 3D), with persistently higher rates and higher-amplitude changes in the western core 2614
283 for most of the time.

284

285 3.3 Foraminiferal Mg/Ca-paleothermometry

286 Prior to elemental analysis, the foraminiferal samples were cleaned following the protocols of
287 Boyle and Keigwin (1985/86) and Boyle and Rosenthal (1996). These include oxidative and
288 reductive (with hydrazine) cleaning steps. Elemental analyses were accomplished with a
289 VARIAN 720-ES Axial ICP-OES, a simultaneous, axial-viewing inductively coupled plasma
290 optical emission spectrometer coupled to a VARIAN SP3 sample preparation system at
291 GEOMAR. The analytical quality control included regular analysis of standards and blanks,
292 with results normalized to the ECRM 752-1 standard (3.761 mmol/mol Mg/Ca; Greaves et al.,
293 2008) and drift correction. The external reproducibility for the ECRM standard was



294 ± 0.01 mmol/mol for Mg/Ca (2σ standard deviation). Replicate measurements reveal a
295 reproducibility of ± 0.28 mmol/mol for *G. truncatulinoides* (2σ standard deviation).
296 *G. truncatulinoides* from core 2614 were only oxidatively cleaned and analyzed on a
297 simultaneous, radially viewing ICP-OES (Ciros CCD SOP, Spectro A.I., Univ. Kiel). A cooled
298 cyclonic spray-chamber in combination with a microconcentric nebulizer (200 μ L/min sample
299 uptake) was optimized for best analytical precision and minimized uptake of sample solution.
300 Sample introduction was performed via an autosampler (Spectra A.I.). Matrix effects caused
301 by varying concentrations of Ca were cautiously checked and found to be insignificant. Drift
302 of the machine during analytical sessions was negligible ($\sim 0.5\%$, as determined by analysis of
303 an internal consistency standard after every 5 samples) (c.f. Nürnberg et al., 2008). To account
304 for the different cleaning techniques prior to Mg/Ca analyses, the initial foraminiferal Mg/Ca
305 data of *G. truncatulinoides* from core 2614 were corrected by 10% according to Barker et al.
306 (2003). See further details and information on contamination and dissolution issues in the
307 Supplement. In the following, species-specific Mg/Ca ratios are termed Mg/Ca_{ruber} ,
308 $Mg/Ca_{universa}$ and $Mg/Ca_{truncatulinoides}$.
309 $Mg/Ca_{universa}$ values were converted into sea surface temperatures ($SST_{Mg/Ca}$) using the species-
310 specific paleotemperature calibration of Hathorne et al. (2003): $Mg/Ca = 0.95 * \exp^{(0.086 * T)}$.
311 This calibration function is based on a North Atlantic core-top calibration study and provides
312 reliable $SST_{Mg/Ca}$ estimates (Supplement Fig. S8, S9) with an error (standard deviation 2σ) of
313 ± 0.2 units of $\ln(Mg/Ca)$, which is equivalent to $\pm 1.1^\circ C$. The calibration provides core-top
314 Holocene (< 10 ka BP) $SST_{Mg/Ca}$ estimates of $\sim 20.5^\circ C$ in the eastern core 2609, and $\sim 19.6^\circ C$ in
315 the western core 2614) (Fig. 4), which are in broad agreement with the modern austral summer
316 SST ranges at 30-80 m water depth in the upper thermocline/mixed layer (see discussion further
317 below; c.f. Supplement Fig. S8, S9). In the case of *G. ruber*, we refrained from converting the
318 Mg/Ca_{ruber} ratios into temperatures due to reasons discussed in the Supplement.
319 The $Mg/Ca_{truncatulinoides}$ values were converted into thermocline temperatures ($TT_{Mg/Ca}$) using
320 the deep-dweller calibration equation of Regenberg et al. (2009): $Mg/Ca = 0.84 * \exp^{(0.083 * T)}$.
321 This calibration provides core-top $TT_{Mg/Ca}$ estimates (on average ~ 10 - $12^\circ C$) (Fig. 5), which
322 agree with the modern annual thermocline temperatures (~ 9 - $12^\circ C$) at the preferred depth of
323 *G. truncatulinoides* (~ 9 - $12^\circ C$) (Fig. 2). The error (standard deviation 2σ) of the calibration is
324 $\pm 1.0^\circ C$. The $TT_{Mg/Ca}$ estimates from other existing paleotemperature calibrations specific to
325 *G. truncatulinoides* are discussed in the Supplement (Fig. S8, S9).
326 For the vertical gradient calculation, we used evenly sampled (200 yrs apart) and linearly
327 interpolated datasets using the software AnalySeries 2.0.8 (Paillard et al., 1996), because



328 foraminiferal specimens were partly too rare not allowing for combined isotope and trace
329 element analyses throughout the entire records, or because data were missing in one or the
330 other record. In particular for core location 2614, negative vertical $\Delta T_{\text{SST-TT}}$ values were
331 interpreted the way that thermocline temperature came close or even became similar to sea
332 surface temperatures (c.f. Fig. 6B). Even though the calibrations were carefully chosen, there
333 remains considerable uncertainty in the absolute temperature values over time. First,
334 calibrations should ideally be region-specific to allow for best reconstructions. None of the
335 calibrations applied, however, were developed for the region south of Australia. Second, the
336 range in downcore temperature amplitudes highly depends on the applied calibration. The less
337 exponential the calibration, the larger the downcore amplitude variations. These
338 imponderabilities cannot be solved in this context.

339

340 **3.4 Stable oxygen isotopes in foraminiferal calcite**

341 Measurements of stable oxygen ($\delta^{18}\text{O}$) and carbon isotopes ($\delta^{13}\text{C}$) on foraminiferal test
342 fragments were performed at GEOMAR on a Thermo Scientific MAT 253 mass spectrometer
343 with an automated Kiel IV Carbonate Preparation Device. The isotope values were calibrated
344 versus the NBS 19 (National Bureau of Standards) carbonate standard and the in-house
345 carbonate standard ‘Standard Bremen’ (Solnhofen limestone). Isotope values in δ -notation are
346 reported in permil (‰) relative to the VPDB (Vienna Peedee Belemnite) scale. The long-term
347 analytical precision is ± 0.06 ‰ for $\delta^{18}\text{O}$ and ± 0.05 ‰ for $\delta^{13}\text{C}$ (1-sigma value). In the
348 following, species-specific $\delta^{18}\text{O}$ values are termed $\delta^{18}\text{O}_{\text{ruber}}$, $\delta^{18}\text{O}_{\text{universa}}$ and $\delta^{18}\text{O}_{\text{trunca}}$.

349

350 **3.5 Oxygen isotope signature of seawater approximating paleo salinity ($\delta^{18}\text{O}_{\text{sw}}$)**

351 Commonly, modern $\delta^{18}\text{O}_{\text{sw}}$ and salinity are linearly correlated in the upper ocean.
352 Unfortunately, the sparse database of modern $\delta^{18}\text{O}_{\text{sw}}$ south of Australia does not allow to
353 accurately describe the relationship (e.g. Schmidt et al., 1999). Past local salinity variations at
354 sea surface and thermocline depths were approximated from $\delta^{18}\text{O}_{\text{sw}}$ derived from combined
355 $\delta^{18}\text{O}$ and $\text{SST}_{\text{Mg/Ca}}$ respective $\text{TT}_{\text{Mg/Ca}}$ measured on the surface and thermocline dwelling
356 foraminiferal species (e.g., Nürnberg et al., 2008; 2015; 2021). First, the temperature effect
357 was removed from the initial foraminiferal $\delta^{18}\text{O}$ by using the temperature versus $\delta^{18}\text{O}_{\text{calcite}}$
358 equation of Bemis et al. (1998) for planktonic foraminifera: $\delta^{18}\text{O}_{\text{sw}} = 0.27 + ((T -$
359 $16.5 + 4.8 * \delta^{18}\text{O}_{\text{foram}}) / 4.8)$. By applying the correction of 0.27 ‰ (Hut, 1987), we converted from
360 calcite on the VPDB scale to water on the Vienna Standard Mean Ocean Water (VSMOW)



361 scale. Second, we calculated the regional ice-volume-free $\delta^{18}\text{O}_{\text{sw}}$ record ($\delta^{18}\text{O}_{\text{sw-ivf}}$) by
362 accounting for changes in global $\delta^{18}\text{O}_{\text{sw}}$, which were due to continental ice volume variability.
363 Here, we applied the Grant et al. (2012) relative sea-level reconstruction to approximate
364 variations in the global ice volume, because it provides a high temporal resolution during MIS
365 3 and times of D/O variability (Fig. 4).

366 The propagated 2σ -error in $\delta^{18}\text{O}_{\text{sw-ivf}}$ is ± 1.16 ‰ for *G. truncatulinoides* (c.f. Reissig et al.,
367 2019) and hence, is larger than for shallow-dwellers (± 0.4 ‰ for *G. ruber*; e.g., Bahr et al.,
368 2013; Schmidt and Lynch-Stieglitz, 2011). The overall Holocene (<10.5 ka BP) $\delta^{18}\text{O}_{\text{sw-ivf}}$
369 amplitude of 1‰ calculated for *O. universa* and *G. truncatulinoides* corresponds to the modern
370 surface $\delta^{18}\text{O}_{\text{sw}}$ variability of ~ -0.5 - 0.5 ‰ for close-to-coast regions south of Australia (Schmidt
371 et al., 1999; c.f. Figs. 2, 4). The calculated mean Holocene (<5 ka BP) surface $\delta^{18}\text{O}_{\text{sw-ivf}}$
372 (*O. universa*) values of 1.2-2 ‰, however, are heavier than the $\delta^{18}\text{O}_{\text{sw}}$ values reported by
373 Richardson et al. (2019) for surface waters (STSW >0.05 ‰). Also, the calculated mean
374 Holocene (<5 ka BP) subsurface $\delta^{18}\text{O}_{\text{sw-ivf}}$ (*G. truncatulinoides*) values of 0.2-0.3 ‰ appear
375 heavier than the reported $\delta^{18}\text{O}_{\text{sw}}$ value for TSAMW (-0.1 to -0.25 ‰) (Richardson et al., 2019).
376 In spite of the potential errors in our $\delta^{18}\text{O}_{\text{sw-ivf}}$ calculations, which are related to i) the large
377 ecological and hydrographical variability and ii) the comparatively large uncertainty of the
378 Mg/Ca-temperature calibrations applied, we note that the relative difference between
379 isotopically heavy STSW and the light TSAMW is well reflected in the calculated sea surface
380 and thermocline $\delta^{18}\text{O}_{\text{sw-ivf}}$ values. The $\delta^{18}\text{O}_{\text{sw-ivf}}$ values were not converted into salinity units,
381 as it is not warranted that the modern linear relationship between $\delta^{18}\text{O}_{\text{sw}}$ and salinity hold
382 through time due to changes in the ocean circulation, and freshwater budget (e.g. Caley and
383 Roche, 2015). We, therefore, interpret the downcore $\delta^{18}\text{O}_{\text{sw-ivf}}$ records as relative variations in
384 salinity.

385

386 4 Results and discussion

387 4.1 Sea surface temperature and salinity development over the last 60 kyrs

388 All raw analytical data of cores 2416 and 2409 versus core depth are presented in the
389 Supplement (Fig. S6, S7). Over the last 60 kyrs, the SST_{Mg/Ca} development in the western and
390 eastern study areas differ substantially. In the western area south of Cape Pasley (core 2614),
391 MIS 3 (~ 57 - 29 ka BP; Lisiecki and Raymo, 2005) is characterized by long-term sea surface
392 warming by on average $\sim 4^\circ\text{C}$ from $\sim 17^\circ\text{C}$ to 21°C until ~ 37 ka BP. This warming trend is
393 underlain by large-amplitude variations in SST_{Mg/Ca} of up to 4 - 5°C , ranging between $\sim 15^\circ\text{C}$
394 and 22°C . The sea surface warming pulses are commonly accompanied by changes to more

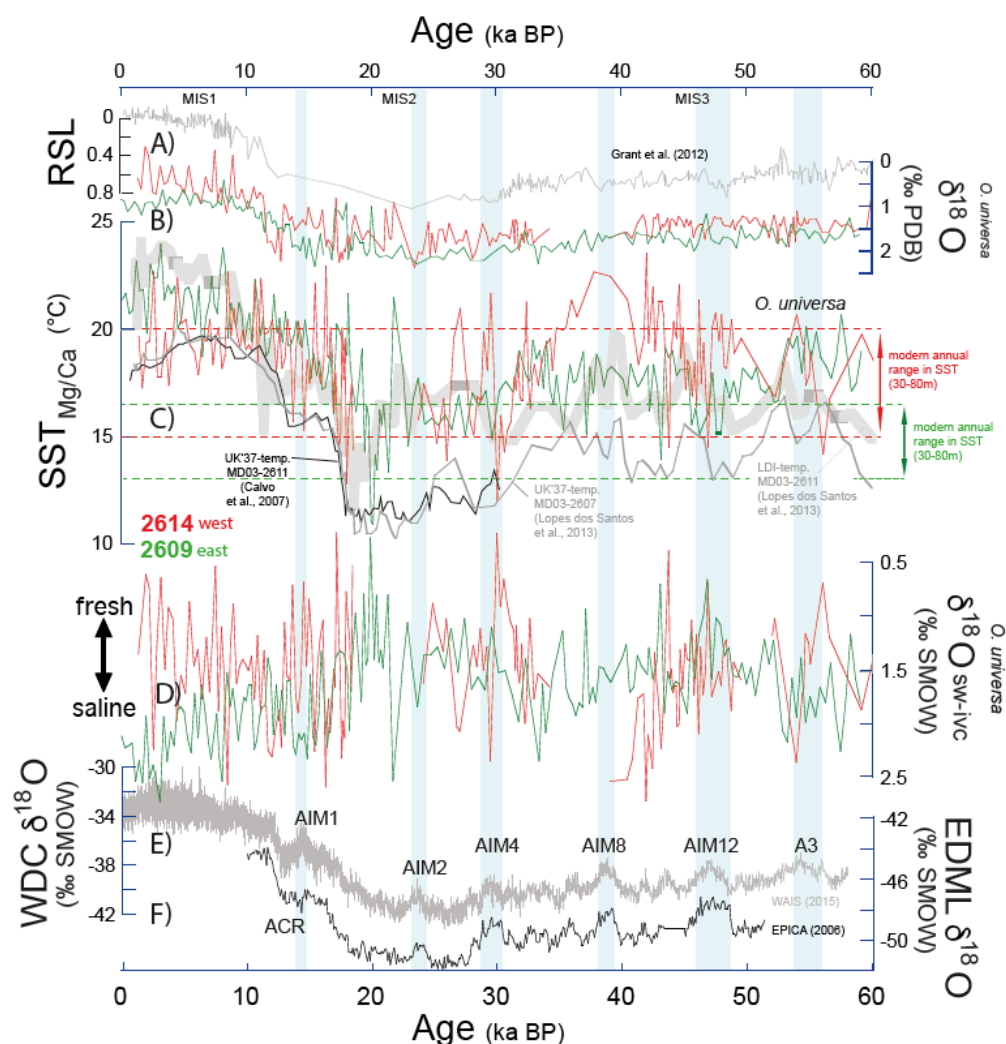


395 saline conditions (high $\delta^{18}\text{O}_{\text{sw-ivc}}$ -values) (Fig. 4). Most of the short-term changes to warm and
396 saline sea surface conditions appear at the Antarctic Warming Events 3 and Antarctic Isotope
397 Maxima (AIM) 12, and 8, and during northern hemisphere cool periods (Fig. 4). These glacial
398 MIS 3 warming pulses compare to and even exceed the modern SST conditions. After ~ 37 ka,
399 the $\text{SST}_{\text{Mg/Ca}}$ decline continuously, accompanied by short-term and high-amplitude warming
400 events rather similar to those events observed during the early MIS3.
401 The subsequent MIS 2 (~ 29 -14 ka BP; Lisiecki and Raymo, 2005) shows rather low $\text{SST}_{\text{Mg/Ca}}$
402 of 14 - 17°C and fresh conditions specifically at the beginning of MIS 2. While *O. universa*
403 specimens are missing during the remaining MIS2, the highly variable $\text{Mg}/\text{Ca}_{\text{G.ruber}}$ data during
404 MIS 2 imply similarly variable $\text{SST}_{\text{Mg/Ca}}$ -conditions as during MIS 3 (see Supplement Fig. S8).
405 During the last deglaciation (~ 18 -12 ka BP), the $\text{SST}_{\text{Mg/Ca}}$ gradually increase from $\sim 15^\circ\text{C}$ to
406 20°C , with intermittent prominent high-amplitude $\text{SST}_{\text{Mg/Ca}}$ variations and maxima of up to
407 $\sim 22^\circ\text{C}$. Similarly, salinity conditions vary considerably ($\delta^{18}\text{O}_{\text{sw-ivc}} = 1.5 \pm 0.5\text{‰}$), with $\delta^{18}\text{O}_{\text{sw-ivc}}$
408 values mostly exceeding the modern values ($>0.05\text{‰}$; Richardson et al., 2019) and pointing
409 to rather saline conditions during times of sea surface warming. The high-amplitude $\text{SST}_{\text{Mg/Ca}}$
410 variations of $\sim 4^\circ\text{C}$ during the Holocene (<10 ka BP) are close to the modern austral summer
411 SST conditions, but in particular during the late Holocene exhibit a slight cooling and
412 freshening trend.
413 In the eastern study area (core 2609) northwest of King Island, the $\text{SST}_{\text{Mg/Ca}}$ range between ~ 16
414 and $\sim 20^\circ\text{C}$ during MIS 3. This is at the upper limit of the modern SST range in this area, which
415 is overall cooler than the western study area. Only temporally $\text{SST}_{\text{Mg/Ca}}$ come close to the core
416 2614 SST conditions. $\text{SST}_{\text{Mg/Ca}}$ amplitudes are approximately half the amplitude observed in
417 the western core 2614. The $\delta^{18}\text{O}_{\text{sw-ivc}}$ variations are rather comparable to those of core 2614,
418 pointing to commonly more saline sea surface conditions than today. Notably, the prominent
419 AIM-related sea surface warming pulses observed in the western core 2614 and the
420 synchronous changes to saline conditions are not seen in core 2609.
421 During the LGM (between ~ 24 ka BP – after HS2 - and 18 ka BP), the $\text{SST}_{\text{Mg/Ca}}$ decline to on
422 average ~ 11 - 16°C , clearly cooler by $\sim 2^\circ\text{C}$ than modern austral winter conditions, and
423 temporally reach values of even $<12^\circ\text{C}$. The $\delta^{18}\text{O}_{\text{sw-ivc}}$ values of 0.5 - 1.5‰ gradually approach
424 the modern values, pointing to fresher conditions when sea surface is cooling. During the
425 deglaciation, the core 2609 $\text{SST}_{\text{Mg/Ca}}$ increase gradually by $>5^\circ\text{C}$, with increasingly saline sea
426 surface conditions. Conditions became relatively similar in both the eastern and western study
427 areas, although remaining more variable in the west (Fig. 4 C).



428 The Holocene SST_{Mg/Ca} in core 2609 increase to ~19-22°C, seemingly warmer and more saline
429 ($\delta^{18}\text{O}_{\text{sw-ivc}} = 1.6\text{-}2.4\text{‰}$) than modern austral summer conditions and those conditions at the
430 western site 2614. This disparity will be discussed further below. We note, however, that the
431 youngest samples in both cores provide rather similar SST_{Mg/Ca} and salinity conditions when
432 relying on the *G. ruber* proxy data (c.f. Supplement Fig. S9: SST_{Mg/Ca} in both cores is 16-18°C,
433 which fairly reflects modern conditions at depths <50 m). We also note that the youngest
434 *O. universa*-derived SST_{Mg/Ca} estimate from core 2609 matches the SST_{LDI} estimate of ~22°C
435 from nearby core MD03-2607 (Lopes dos Santos et al., 2013; close to the Murray Canyon;
436 36°57.64'S 137°24.39'E)) (Fig. 4 C). The SST_{LDI} estimates are based on long-chain diols, and
437 LDI-inferred temperatures supposedly reflect SSTs of the warmest month (Lopes dos Santos
438 et al., 2013). We hence hypothesize that the *O. universa* SST_{Mg/Ca} signal is seasonally biased
439 towards the austral summer season. We note also that the entire core 2609 SST_{Mg/Ca} record
440 matches the SST_{LDI} record from nearby core MD03-2607 reasonably well, with similar
441 absolute temperature estimates (~11-24°C) and in particular, similar deglacial amplitudes of
442 up to 7°C (Fig. 4 C). Both, the SST_{LDI} and SST_{Mg/Ca} estimates are warmer by 4°C than the
443 alkenone-based SST_{U^k₃₇} estimate from cores MD03-2607 (Lopes dos Santos et al., 2012) and
444 MD03-2611 (Calvo et al., 2007; 36°44'S, 136°33'E) (Fig. 1), likely due to the fact that SST_{U^k₃₇}
445 reflect the cooler early spring conditions.

446 The core 2614 SST_{Mg/Ca} record broadly follows the Clement et al. (1999) modelled El Niño-
447 Southern Oscillation (ENSO) power (c.f. Tudhope et al., 2001) (Fig. 6), relating the enhanced
448 SST conditions at core 2614 to weak ENSO conditions (= strong La Niña) in line with high sea
449 level anomalies, strengthened Leeuwin Current volume transport,



450
 451 **Figure 4. Hydrographic development at sea surface over the last 60 kyr.** Colored curves = this study, gray
 452 and black curves = reference records. A) Relative sea level curve of Grant et al. (2012), in ‰. B) Sea surface
 453 $\delta^{18}\text{O}_{O.universa}$ records at the western (red; core 2614) and the eastern (green; core 2609) core locations. C) $\text{SST}_{\text{Mg/Ca}}$
 454 records derived from *O. universa* (red: core 2614; green: core 2609). The long-chain diol-based SST_{LDI} (thick
 455 gray) and alkenone-based SST_{UK37} records (thin gray and black) of nearby cores MD03-2607 and MD03-2611
 456 (Calvo et al., 2007; Lopes dos Santos et al., 2013) are for comparison. D) Relative sea surface salinity
 457 approximations ($\delta^{18}\text{O}_{\text{sw-ive}}$) at the western (red) and eastern (green) core locations. E) West Antarctic Ice Sheet
 458 Divide Core (gray; WAIS Divide Project Members, 2015) and the EDML (black; EPICA Group Members, 2006)
 459 $\delta^{18}\text{O}$ records as reference for the southern hemisphere climate signal. Blue shadings = Antarctic Isotope Maxima
 460 (AIM). Dashed red and green lines = modern annual SST range at 50-100 mwd at eastern and western cores 2609
 461 and 2614; WOA, Locarnini et al., 2018. MIS = Marine Isotope Stages 1-3 (Martinson et al., 1987).
 462



463 eddy energetics, and the poleward transport of warm waters (Pearce and Phillips, 1988; Feng
464 et al., 2003; Wijffels and Meyer, 2004; Middleton and Bye, 2007; Pattiaratchi and Siji, 2020)
465 (Fig. 5 A). The correlation cannot be expected to be one-to-one, as the SST signal off Cape
466 Pasley is biased and experienced (austral summer) contributions of high-salinity South Indian
467 Central Water (SICW) (Cresswell and Peterson, 1993). However, as the Leeuwin Current is
468 mainly fed by low-salinity and nutrient-depleted waters from the Indo-Pacific Warm Pool
469 (Meyers et al., 1995; Domingues et al., 2007), and as its modern dynamic evolution is clearly
470 linked to ENSO being weaker during El Niño years (3 Sv) and stronger during La Niña years
471 (4.2 Sv) (Feng et al., 2003), we argue that ENSO was effectively shaping the Leeuwin Current
472 even during the rapid climatic changes of MIS3.

473

474 **4.2 Thermocline temperature and salinity development over the last 60 kyrs**

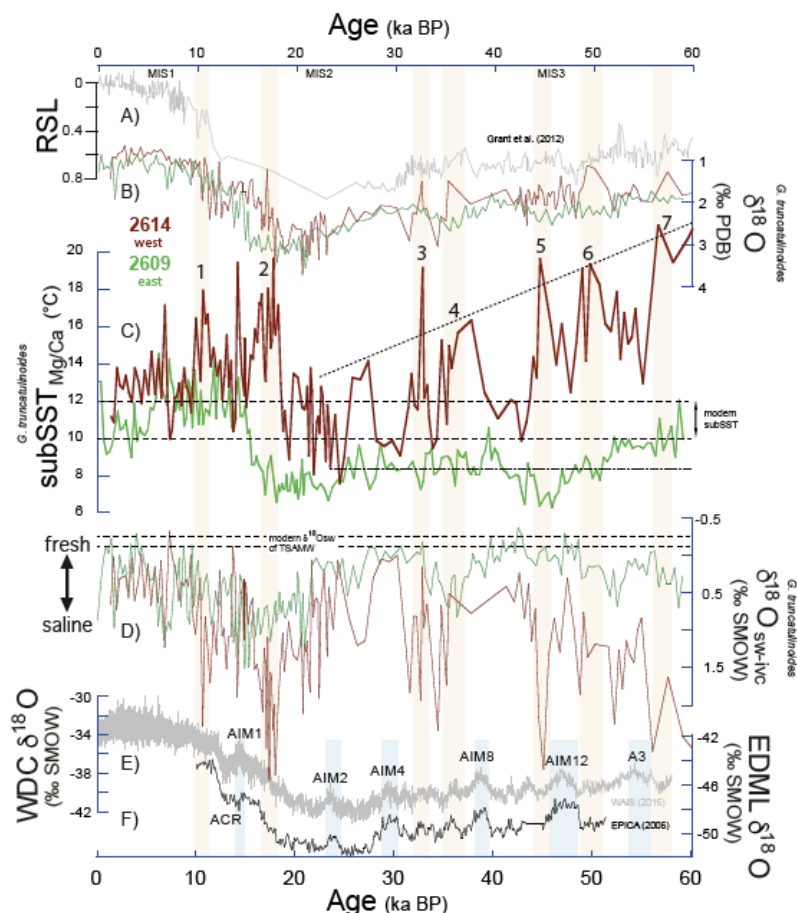
475 All raw analytical data of cores 2614 and 2609 versus core depth are presented in the
476 Supplement (Fig. S6, S7). Over the last 60 kyrs, the development at thermocline depth in the
477 western study area south of Cape Pasley (core 2614) differs substantially from the eastern area,
478 with prominent and rapid high-amplitude changes in $TT_{Mg/Ca}$ and the according $\delta^{18}O_{sw-ivc}$ in the
479 western area. The proxy records from the eastern core 2609, instead, appear rather muted,
480 cooler and fresher (Fig. 5 C, D).

481 During MIS 3, the $TT_{Mg/Ca}$ in western core 2614 range between $10^{\circ}C$ and $21^{\circ}C$, revealing a
482 long-term cooling trend from on average $\sim 18^{\circ}C$ at 60 ka BP to $\sim 11^{\circ}C$ at ~ 23 ka BP. This
483 cooling trend is accompanied by high-amplitude $TT_{Mg/Ca}$ variations even exceeding $5^{\circ}C$. The
484 $TT_{Mg/Ca}$ and thermocline depth $\delta^{18}O_{sw-ivc}$ minima correspond to the modern TT and $\delta^{18}O_{sw}$
485 ranges at site 2614, while distinct warming pulses at thermocline depth along with saline
486 conditions exceed modern conditions by up to $\sim 10^{\circ}C$ and ~ 2 ‰, respectively (Fig. 5 C, D).
487 Although some of these $TT_{Mg/Ca}$ warming pulses are only represented by single Mg/Ca-data
488 points (due to rare foraminiferal sample material), we assess them as robust as the peaks are
489 mostly supported by several $\delta^{18}O_{G.truncatulinoides}$ and $\delta^{13}C_{G.truncatulinoides}$ -excursions to light values
490 (Fig. 5 B).

491 In the eastern core 2609, the MIS3 $TT_{Mg/Ca}$ range between $\sim 7^{\circ}C$ and $10^{\circ}C$, which is cooler by
492 ~ 2 - $3^{\circ}C$ than the modern TT range. The thermocline depth $\delta^{18}O_{sw-ivc}$ values are mostly equal or
493 more negative (-0.5 - 0.5 ‰) than the modern value, implying clearly fresher conditions and less
494 variability than at the western core (0 - 2 ‰). During MIS 2 and in particular during the LGM,
495 the conditions at thermocline depth at core 2609 are cooler-than-modern by $\sim 2^{\circ}C$, fresher, and
496 low in amplitude compared to the clearly more variable and warmer thermocline conditions at



497 core 2614 (Fig. 5 C, D). The western location rather exhibits short-term $TT_{Mg/Ca}$ variations
498 between 8°C and 13°C, which is close to the modern TT in the region. Relative salinity varied
499 correspondingly (0.5-1.5‰).



500
501 **Figure 5. Hydrographic development at thermocline depth over the last 60 kyr.** Colored curves = this study,
502 gray and black curves = reference records. A) Relative sea level curve of Grant et al. (2012), in ‰. B) Thermocline
503 $\delta^{18}O_{G.truncatulinooides}$ records at the western (brown; core 2614) and the eastern (green; core 2609) core locations. C)
504 $TT_{Mg/Ca}$ records derived from *G. truncatulinooides* (brown: core 2614; green: core 2609). D) Thermocline salinity
505 approximations ($\delta^{18}O_{sw-ivc}$) at the western (brown) and eastern (green) core locations. The modern $\delta^{18}O_{sw}$ -range of
506 TSAMW is indicated by stippled lines (Richardson et al., 2019). E) West Antarctic Ice Sheet Divide Core (gray;
507 WAIS Divide Project Members, 2015) and F) EDML (black; EPICA Group Members, 2006) $\delta^{18}O$ records as
508 reference for the southern hemisphere climate signal. Blue shadings = Antarctic Isotope Maxima (AIM). Red
509 shadings = prominent thermocline warming pulses and changes to high salinities at thermocline depth (black
510 numbers). Dashed lines = modern annual TT range at 50-100 mwd; WOA (Locarnini et al., 2018), and modern
511 $\delta^{18}O_{sw}$ (Schmidt et al., 1999). MIS = Marine Isotope Stages 1-3 (Martinson et al., 1987); ACR = Antarctic Cold
512 Reversal.



513 In the western study area, the deglaciation is characterized by rapid and prominent changes in
514 thermocline conditions (Fig. 5 C). Increases in $TT_{Mg/Ca}$ by up to $10^{\circ}C$ to max. $20^{\circ}C$, and in
515 $\delta^{18}O_{sw-ivc}$ by up to 2.5‰ in amplitude occur during the early Heinrich Stadial 1, the early
516 Bølling/Allerød, and the Preboreal. In contrast, the deglacial change in the eastern study area
517 lags the western development and is less prominent, with $TT_{Mg/Ca}$ rising from $7^{\circ}C$ to $12^{\circ}C$ in
518 line with the Southern Hemisphere deglacial climate change as reflected in the EDML $\delta^{18}O$
519 record (EPICA Group Members, 2006) (Fig. 5 C).

520 The Holocene is characterized in both regions by subtle variations in $TT_{Mg/Ca}$ and
521 corresponding $\delta^{18}O_{sw-ivc}$. The western core shows higher $TT_{Mg/Ca}$ ($\sim 12\text{--}14^{\circ}C$ and warmer-than-
522 modern conditions) than the eastern core ($\sim 10\text{--}12^{\circ}C$, rather similar to modern conditions at
523 thermocline depth), while the salinity ($0\text{--}0.5\text{‰}$) in both areas appears rather similar and close
524 to the modern values (which is $34.8\text{--}35.1$ in the western core and $34.7\text{--}34.9$ in the eastern core)
525 (Fig. 5 C, D).

526

527 **4.3 Sea surface - thermocline interrelationships reflecting Leeuwin Current dynamics**

528 We interpret the SST and surface $\delta^{18}O_{sw-ivc}$ data derived from *O. universa* in terms of changes
529 in the surface mixed layer, which is dominated by STSW (contributions of Leeuwin Current-
530 transported TSW, and South Indian Ocean Current-transported SICW) at the western core
531 locations and by the South Australian Current (SAC) in the eastern study area (Fig. 1). The
532 thermocline-dwelling *G. truncatulinoides* proxy data, instead, reveal changes in the underlying
533 Central Water, which comprises SABCW and Tasman Subantarctic Mode Water (TSAMW).
534 According to Richardson et al. (20019), the boundary between STSW and Central Water (in
535 particular the top surface of SABCW) along the southern Australian margin defines the
536 interface between the eastward-directed Leeuwin Current System transporting subtropical
537 waters and the westward flow of the Flinders Current System, which brings subantarctic waters
538 into the region (SABCW coupled to TSAMW and Tasmanian Intermediate Water (TIW)) (Fig.
539 2 B).

540 To assess the dynamics of the Leeuwin Current-transported STSW and its interaction with both
541 the surface SAC and the underlying SABCW/TSAMW south of Australia through time, we
542 calculated the vertical temperature gradients at both core locations (c.f. Methods). The vertical
543 temperature gradient (ΔT_{SST-TT}) provides insight into the thermocline depth, with low (high)
544 ΔT_{SST-TT} pointing to a deep (shallow) thermocline with accompanying strong (weak)
545 stratification. In conjunction with the lateral gradients at both sea surface ($\Delta SST_{west-east}$) and
546 thermocline depths ($\Delta TT_{west-east}$) (Fig. 6), which define the regional differences at the two depth



547 levels, we derive insight on how the Leeuwin Current System developed spatially in relation
548 to the Flinders Current System during different climate regimes. The similarity ($R = 0.87$) of
549 the $\Delta T_{\text{west-east}}$ -record (Fig. 6) and the $T_{\text{Mg/Ca}}$ -record of the western core 2614 (Fig. 5)
550 pinpoints that it is the thermocline changes in the western area, which are crucial to the
551 oceanographic setting south of Australia, and which best reflect the relative presence of the
552 different water masses.

553 The latest Holocene $\Delta T_{\text{west-east}}$ and $T_{\text{Mg/Ca}}$ -data ($< 2\text{ka BP}$) suggesting warmer-by- 2°C $SST_{\text{Mg/Ca}}$
554 and a shallower thermocline in the east, and slightly warmer-by- 1°C $T_{\text{Mg/Ca}}$ in the west (Fig.
555 6) compare to the modern situation: During austral autumn and winter, the Leeuwin Current-
556 transported STSW is thicker ($\sim 300\text{ m}$ in the western and $\sim 200\text{-}250\text{ m}$ in the eastern study area;
557 Richardson et al., 2019) with a rather equalized vertical temperature gradient in the west (Fig.
558 2). When opposing winds cease, it reaches further to the east due to a strong Zeehan Current
559 adjoining the Leeuwin Current (Cresswell, 2000; Ridgway and Condie, 2004; Ridgway, 2007)
560 and causes warming at depth. During austral summer (November to March), the STSW is at
561 shallower depths ($\sim 200\text{-}250\text{ m}$ in the west and $\sim 150\text{-}50\text{ m}$ in the east; Richardson et al., 2019)
562 (c.f. Fig. 2) with a well-defined shallow thermocline during times of a weak Leeuwin Current,
563 when opposing winds (blowing from the southwest northwards) are strong (Godfrey and
564 Ridgway, 1985; Smith et al., 1991; Feng et al., 2003; 2009).

565 *MIS3*

566 The oceanographic setting as existent today was considerably different during the early MIS3
567 with tangible differences between both regions. The thermocline was generally deeper (Fig. 6
568 B), and the sea surface and thermocline waters were considerably warmer and more saline in
569 the western than in the eastern region (Figs. 4, 5), pointing to an overall thick STSW in line
570 with a strong Leeuwin Current. In the western core 2614, we observe five time periods of
571 thermocline warming and deepening during the extreme cool climate conditions in Antarctica
572 (c.f. EPICA, 2006; WAIS Divide Project Members, 2015 climate records): $\sim 58.8\text{-}55.8\text{ ka BP}$,
573 $\sim 50.8\text{-}48.4\text{ ka BP}$, $\sim 46.6\text{-}44.2\text{ ka BP}$, $\sim 37.4\text{-}34.2\text{ ka BP}$, $\sim 33.0\text{-}31.4\text{ ka BP}$ (termed 7 to 3 in
574 Figs. 5 C, 6 C). These warm events at thermocline depth were likely related to the strong
575 southward transfer of tropical heat *via* the Leeuwin Current and the poleward dislocation of the
576 STF. On average, they become cooler towards the younger part of the core, supporting the
577 notion of i) a gradually shoaling thermocline depth ($\Delta T_{\text{SST-TT}}$) at the western core 2614, and ii)
578 the narrowing of the lateral temperature gradient at thermocline depth ($\Delta T_{\text{west-east}}$) from on
579 average 13°C to 3°C during the course of MIS3 (Fig. 6 C). Fig. 7 A illustrates the straight
580 relationship between $\Delta T_{\text{SST-TT}}$ and $\Delta T_{\text{west-east}}$ for core 2614.



581 Overall, the rapidly developing (within centuries) thermocline warming events are intercalated
582 by times of cool, fresh, and shallow thermocline conditions. These conditions predominated
583 during Antarctic Isotope Maxima (A3, AIM12, AIM11, and AIM 4) when in particular the sea
584 surface experienced warming by a couple of degrees, pointing to the presence of a shallow and
585 weak Leeuwin Current in the west rather analogous to a modern austral summer scenario (Fig.
586 6 A).

587 We argue that the highly variable sea surface and thermocline conditions during MIS3 were
588 likely related to rapid shifts of the oceanic and atmospheric frontal systems: i) The poleward
589 movement of the Subtropical Ridge and STF promoting an enhanced STSW contribution in
590 relation to a stronger Leeuwin Current, and ii) the successive equatorward frontal migration
591 leading into the full glacial conditions with an overall weak Leeuwin Current (see discussion
592 below). This is in line with Moros et al. (2009) and De Deckker et al. (2012), who related
593 reduced (increased) Leeuwin Current strength to the northward (southward) displacement of
594 the STF prompted by the strengthening (weakening) of the westerlies in response to changing
595 low to high latitude pressure and thermal gradients. The comparison to the Wu et al. (2021)
596 proxy record of bottom current strength in the Drake Passage (Fig. 8 C) further illustrates that
597 times of a strong Leeuwin Current (thermocline warming events 7 to 3; orange shading in Fig.
598 8) were mostly accompanied by a weakly developed ACC. A weak Leeuwin Current, instead
599 predominated during times of ACC acceleration to higher flow speeds during warm intervals
600 in the Southern Hemisphere (A3, AIM12, AIM11, and AIM 4).

601 Strength variations in the ACC are commonly attributed to changes of the Southern Westerly
602 Wind Belt (SWW; Lamy et al., 2015) associated with northward shifts of the Subantarctic
603 Front (Roberts et al., 2017). However, model simulations (Gottschalk et al., 2015) imply that
604 changes in the westerlies alone were likely insufficient to influence high-amplitude changes in
605 ACC speeds (Gottschalk et al., 2015). Wu et al. (2021), recently, suggested that the millennial-
606 scale ACC flow speed variations were closely linked to variations of Antarctic sea ice extent
607 (maxima in ACC strength at major winter sea ice retreat; weaker ACC at a more extensive sea
608 ice cover), closely related to the strength and latitudinal position of the SWW (Toggweiler et
609 al., 2006), oceanic frontal shifts (Gersonde et al., 2005), and buoyancy forcing (Shi et al.,
610 2020).

611 At the eastern core location 2609, the thermocline and halocline changes vary only marginally
612 ($TT_{Mg/Ca}$ amplitude of $\sim 3^{\circ}\text{C}$ compared to $>10^{\circ}\text{C}$ at the western site; $\delta^{18}\text{O}_{\text{sw-ivc}}$ amplitude of $\sim 1\text{‰}$
613 compared to $>3\text{‰}$ at the western site) with no apparent relationship to the short-term MIS3
614 climate variability (which is likely due to our partly incomplete sampling) (Fig. 5 C, D). The



615 relationship between $\Delta T_{\text{SST-TT}}$ and $\Delta T_{\text{west-east}}$ is not well expressed, and clearly different from
616 core 2614 (Fig. 6 B, C; Fig. 7). We note that even during most intensive STSW transport *via*
617 the Leeuwin Current during the MIS 3 thermocline warming periods 7, 6, 5, 4, 3, the eastern
618 core location was hardly affected. We speculate that the Leeuwin Current (defined by Ridgway
619 and Condie, 2004 as “southward shelf edge flow off western Australia that turns around Cape
620 Leeuwin and penetrates eastward as far as the central Great Australian Bight”) was not present
621 at the core 2609 location at all. Instead, it is likely the South Australian Current (defined by
622 Ridgway and Condie, 2004 as “winter shelf edge flow largely driven by reversing winds ...
623 that originates from a gravity outflow from the eastern Great Australian Bight and spreads
624 eastward as far as the eastern edge of Bass Strait”), which determines when the core 2609
625 $\text{SST}_{\text{Mg/Ca}}$ approach those of core 2614. Rather equalized $\text{SST}_{\text{Mg/Ca}}$ conditions at both study sites
626 with according $\Delta \text{SST}_{\text{Mg/Ca}}$ minima occurred consistently during the MIS 3 warming periods 7,
627 6, 5, 4, 3, implying that the formation of the South Australian Current intensified at times of a
628 strong Leeuwin Current (Fig. 6 C).

629 The differences in thermocline development at both core locations might have been fostered
630 by the functioning of the Subtropical Ridge, a belt of high-pressure systems (anticyclones)
631 dividing the tropical south-easterly circulation (trade winds) from the mid-latitude westerlies.
632 The Subtropical Ridge is shaped by the Indian Ocean Dipole and the Southern Annual Mode,
633 and to a lesser degree by ENSO (Cai et al., 2011). During austral autumn/winter (austral
634 spring/summer), it moves north (south), allowing the westerlies to seasonally strengthen
635 (weaken) rainfall in SE Australia (Cai et al., 2011). During El Niño conditions, the Subtropical
636 Ridge is displaced farther equatorward than normal, while during La Niña conditions it is
637 shifted poleward (Drosowsky, 2003). Today, the Subtropical Ridge lies between $\sim 30^\circ\text{S}$ and
638 $\sim 40^\circ\text{S}$ (e.g., Drosowsky, 2005). We therefore argue that the eastern core 2609 at $\sim 39^\circ\text{S}$ is
639 more effectively influenced by temporal and spatial changes in the Subtropical Ridge as being
640 closer to the rainy westerlies than the western core 2614 at $\sim 34^\circ\text{S}$. Congruently, the core 2609
641 surface and thermocline $\delta^{18}\text{O}_{\text{sw-ivc}}$ -records point to overall fresher sea surface conditions during
642 MIS3 cool periods than core 2614. A new pollen record from in between our core locations
643 (DeDeckker et al., 2021; core MD03-2607; Fig. 1) does unfortunately not capture the rapid
644 MIS 3 variability we see in our oceanographic reconstructions, although revealing subtle
645 changes in regional vegetation and fluvial discharge patterns in the Murray Darling Basin.
646

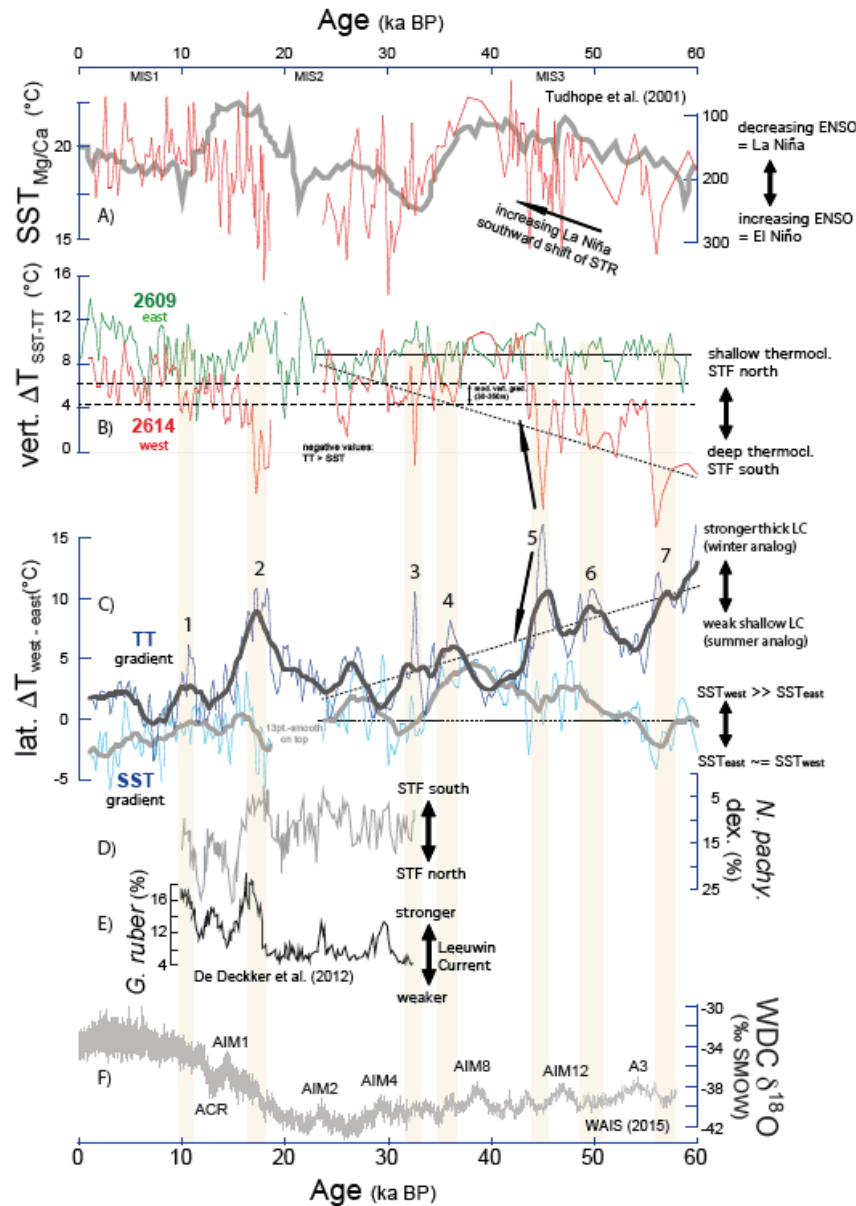


647 *LGM*

648 At the western core location 2614, the few but relatively heavy $\delta^{18}\text{O}_{\text{universa}}$ data point to rather
649 cool sea surface conditions during the Last Glacial Maximum (LGM) (Fig. 4 B, 6 A). The
650 thermocline conditions ($\sim 8\text{-}13^\circ\text{C}$) appear cool but variable (Fig. 5 C). At the eastern core
651 location 2609, instead, the thermocline was even cooler, cooler-than-modern by $\sim 2^\circ\text{C}$, fresher,
652 and low in amplitude. Overall, we note a shallow thermocline and an equalized West-East
653 gradient at thermocline depth, pointing to a narrower, shallower and weaker Leeuwin Current
654 influencing the western study area. This is in accordance with Martinez et al. (1999), who
655 described the northward dislocation and shrinking of the Indo-Pacific Warm Pool during the
656 LGM, which should have significantly reduced the export of tropical low saline and warm ITW
657 water *via* the Leeuwin Current, and consequently, should have reduced the geostrophic gradient
658 similar to El Niño conditions (Meyers et al., 1995; Feng et al., 2003).

659 The northward movement of the STF (Howard and Prell, 1992; Martinez et al., 1997; Passlow
660 et al., 1997; Findlay and Flores, 2000; Nürnberg and Groeneveld; 2006) and the northward
661 shift of the Subtropical Ridge by $2\text{-}3^\circ$ latitude (Kawahata, 2002) during full glacial climate
662 conditions likely strengthened the West Australian Current as eastern boundary current,
663 introducing higher portions of cool SICW into the Leeuwin Current (Wandres, 2018; Barrows
664 and Juggins, 2005). The enhanced glacial dominance of the West Australian Current implies
665 that either wind conditions became favorable for its flow, and/or the alongshore geopotential
666 pressure gradient, which drives the Leeuwin Current, was exceeded by the wind stress from the
667 coastal southwesterly winds (Wandres, 2018; Spooner et al., 2011). The resulting glacial
668 reduction of southward heat transfer should have resulted in the significant reduction of cloud
669 cover, and hence precipitation. Courtillot et al. (2020) noted that today's rainfall is more
670 important in the cool winter months, when the subtropical highs (or subtropical ridges) move
671 to the north and the cold fronts embedded in the westerly circulation bring moisture over the
672 continent (McBride, 1987; Suppiah, 1992).

673 At the eastern core location 2609, the relatively fresh and cool conditions at both surface and
674 thermocline depth, the shallow thermocline, and the small $\Delta T T_{\text{West-East}}$ gradient at times of a
675 narrower and shallower Leeuwin Current (Fig. 6) rather imply that during the LGM i) the
676 formation of the South Australian Current was rather inactive and ii) SABCW increasingly
677 formed along the northerly displaced STF by convective overturning and subduction
678 (Richardson et al., 2018) during times of intensified westerlies (e.g. Kaiser and Lamy, 2010),
679 and was carried northward by a glacially strengthened Flinders Current.



680
 681 **Figure 6. Variability of lateral and vertical temperature gradients south of Australia** in comparison to other
 682 proxy records over the last 60 kyr. A) Western core 2614 SST_{Mg/Ca} record (red) underlain by the ENSO-strength
 683 (gray; dimensionless) of Tudhope et al. (2001). The ENSO strength was simulated using the Zebiak–Cane coupled
 684 ocean–atmosphere model forced by changing orbital parameters. Higher power inference suggests more El Niño
 685 events causing drier-than-normal conditions over northern Australia, Indonesia and the Philippines (c.f. Saltré et
 686 al., 2016). B) Vertical temperature gradients (ΔT_{SST-subSST}) between sea surface and thermocline reflecting
 687 thermocline changes in the western (red) and eastern (green) study areas. Hatched lines mark the modern vertical



688 gradient in the west (WOA, Locarnini et al., 2018). C) Lateral (west-east) 7-point-smoothed temperature gradients
689 at sea surface (gray) and at thermocline depth (black), underlain by the raw data, reflecting Leeuwin Current
690 strength. Stippled lines in B) and C) indicate long-term trends. D) *N. pachyderma* dextral and E) *G. ruber*
691 percentages of core MD03-2607 from De Deckker et al. (2012) reflecting lateral migrations of the STF and
692 changes in Leeuwin Current strength, respectively. F) West Antarctic Ice Sheet Divide Core $\delta^{18}\text{O}$ record (WAIS
693 Divide Project Members, 2015) as a reference for the southern hemisphere climate signal. Orange shading = short
694 time periods of a strong Leeuwin Current. A3 = Antarctic warming event; AIM = Antarctic Isotope Maxima; MIS
695 = Marine Isotope Stages 1-3 (Martinson et al., 1987); ACR = Antarctic Cold Reversal.

696

697 Our marine proxy records allow to draw new conclusions on the oceanic and climatic evolution
698 south of Australia during MIS3 and 2, which confirms but also adds to the climatic information
699 available from low-resolution Australian terrestrial records. Petherick et al. (2013) concluded
700 from a large compilation of vegetational data that the glacial climate of the Australian
701 temperate region was relatively cool with the expansion of grasslands and increased fluvial
702 activity in the Murray-Darling Basin, likely in response to a northerly shift of the Southern
703 Ocean oceanic frontal system. Expanded sea ice around Antarctica, and a concomitant influx
704 of subantarctic waters along the southeast and southwest Australian coasts occurred at the same
705 time. Notably, the cooling and aridification in Australia during the LGM led to (c.f. DeDeckker
706 et al., 2021; core MD03-2607; Fig. 1) pronounced geographic contractions of human
707 populations and abandonment of large parts of the continent (Williams et al., 2013), followed
708 by a deglacial re-expansion of populations (Tobler et al., 2017).

709 *Deglaciation*

710 The deglacial warming in Antarctica was accompanied by sea ice retreat, sea level rise, and
711 rapidly increasing SSTs in the Southern Ocean between ~ 18 and 15 ka BP (Barrows et al.,
712 2007; Pedro et al., 2011). In both our cores, the beginning of the deglaciation is defined by the
713 common decline in planktonic $\delta^{18}\text{O}$ -values (*G. ruber*, *O. universa*, *G. truncatulinoides*)
714 starting at ~ 18 ka BP (Fig. 3). It is further characterized by sea surface warming closely related
715 to the southern hemisphere climate signal (WAIS Divide Project Members, 2015; EPICA,
716 2006) (Fig. 3) with $\text{SST}_{\text{Mg/Ca}}$ being overall warmer in the western core region, and rather
717 congruent to other deglacial SST proxy records from the region (Fig. 4 B, C; Lopes dos Santos
718 et al., 2013; Calvo et al., 2007).

719 The deglacial thermocline development, however, differs between core locations, with a rapid
720 (within a few centuries) and variable change to high $\text{TT}_{\text{Mg/Ca}}$ and high salinities from ~ 18.3 -
721 15.8 ka BP in the western area, similar to the thermocline deepening and warming episodes
722 described earlier for MIS3 (Fig. 5). The enhanced vertical ($\Delta T_{\text{SST-TT}}$) and lateral temperature



723 gradients ($\Delta T_{\text{West-East}}$) (Fig. 6) point to the rapid formation of a deep thermocline in response to
724 a strengthened Leeuwin Current, and the greater influx of ITW waters at the expense of SICW
725 contributions during the times of poleward migration of the STF. A second major, although
726 less prominent advance of the Leeuwin Current took place at $\sim 11.1-9.9$ ka BP before relatively
727 weak Holocene conditions were achieved. These deglacial intensifications of the Leeuwin
728 Current were synchronous to foraminiferal assemblage changes detected by De Deckker et al.
729 (2012) on Great Australian Bight core MD03-2611 (c.f. Fig. 1), which were interpreted in terms
730 of southward migrations of the STF (Fig. 6 D, E).

731 At the eastern core 2609, the prominent deglacial changes in the thermocline are missing,
732 suggesting that the Leeuwin Current did not reach the eastern study area (Figs. 4, 5). Slight
733 increases in $SST_{\text{Mg/Ca}}$ during these short time periods of a strong Leeuwin Current imply that
734 the formation of the South Australian Current might have been active though. The vegetational
735 record from the Australian temperate region showing the expansion of arboreal taxa at the
736 expense of herbs and grasses points to a gradual deglacial ($\sim 18-12$ ka BP) rise in air
737 temperature and precipitation in the Murray-Darling Basin, and the strengthened influence of
738 the westerlies across the southern Australian temperate zone (Fletcher and Moreno, 2011).

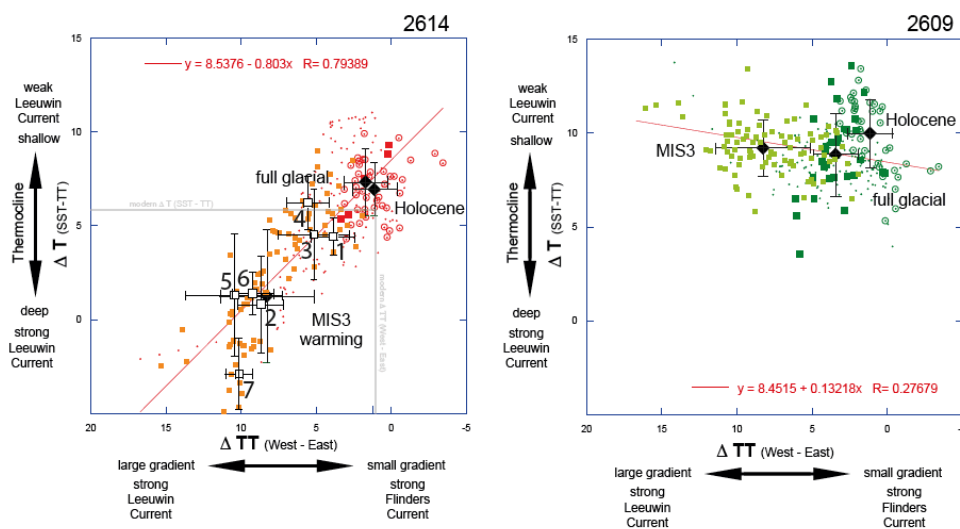
739 *Holocene*

740 The oceanographic development during the Holocene closely corresponds to the vegetational
741 and climatic development of Australia. Most importantly, the thermocline off S Australia was
742 considerably shallower during the Holocene compared to the prominent MIS3 and deglacial
743 periods of Leeuwin Current intensification, pointing to a comparably weak Leeuwin Current
744 (Fig. 6). At the sea surface, the eastern study area was apparently warmer and more saline than
745 the western area (Fig. 4 B). On land, Petherick et al. (2013) described an early Holocene
746 expansion of sclerophyll woodland and rainforest taxa across the Australian temperate region
747 after ~ 12 ka BP, which they related to increasing air temperature and a spatially heterogeneous
748 hydroclimate with increased effective precipitation (c.f. Williams et al., 2006; Kiernan et al.,
749 2010; Moss et al., 2013), a widespread re-vegetation of the highlands, and a return to full
750 interglacial conditions. At the same time, the East Australian Current re-invigorated flowing
751 south down the east coast of Australia and seasonally affecting the south coast (Bostock et al.,
752 2006).

753 The differential behaviour at surface and thermocline depths became most pronounced after ~ 6
754 ka BP, when the thermocline at the eastern core location 2609 became distinctly shallower than
755 in the western study area, while $SST_{\text{Mg/Ca}}$ continued to increase. We relate the warmer and more



756 saline late Holocene conditions at sea surface in the east (Fig. 4 B, D) to intensified surface
757 heating near the eastern edge of the Great Australian Bight during austral summer (c.f.
758 Herzfeld, 1997). These shallow waters then spread eastward over the shelf and continued to
759 flow as South Australian Current towards Bass Strait (Middleton and Platov, 2003; Ridgeway
760 and Condie, 2004) (c.f. Fig. 1). Also after ~6 ka, Petherick et al. (2013) describe a higher
761 frequency climatic variability in the Australian temperate region and a spatial patterning of
762 moisture balance changes that possibly reflect the increasing influence of ENSO climate
763 variability originating in the equatorial Pacific (Moy et al., 2002).



764
765 **Figure 7. Vertical temperature versus lateral thermocline temperature gradient as expression of Leeuwin**
766 **Current System variability.** The vertical temperature gradient (ΔT_{SST-TT}) provides insight into the thermocline
767 depth, with low (high) ΔT_{SST-TT} pointing to a deep (shallow) thermocline. The lateral gradient at thermocline depth
768 ($\Delta TT_{west-east}$) defines how the Leeuwin Current developed in relation to the Flinders Current. Left: western core
769 2614 showing a well-defined relationship between ΔT_{SST-TT} and $\Delta TT_{west-east}$ ($R = 0.8$). Prominent MIS3
770 thermocline warming periods (orange symbols; white squares = averages, numbered from 7 to 1) point to a strong
771 Leeuwin Current, which weakened across MIS3 (black diamond = average) approaching LGM (red squares) and
772 Holocene conditions (red circles; black diamonds = averages). Right: eastern core 2609 lacks a relationship
773 between ΔT_{SST-TT} and $\Delta TT_{west-east}$, implying that the Leeuwin Current is not affecting this study site over time.
774



775 At thermocline depth, the development of gradually declining $TT_{Mg/Ca}$ and salinities appear
776 rather similar in the eastern and western study areas over the Holocene, although the western
777 area remained warmer by $\sim 2^{\circ}\text{C}$ and the thermocline was deeper due to an active but relatively
778 weak Leeuwin Current (Fig. 5 C, D). These conditions gradually approached the modern
779 situation, and imply a strengthened influence of the SABCW and SAMW in the course of the
780 Holocene, transported by an intensified Flinders Current/Leeuwin Undercurrent system. The
781 eastern study area was more affected, likely because the Subtropical Ridge gradually shifted
782 northward across the core 2609 location in response to the increasing influence of ENSO
783 climate variability. From geochemical proxy data of annually banded massive *Porites* corals
784 from Papua New Guinea, Tudhope et al. (2001) concluded that ENSO developed from weak
785 conditions in the early to mid-Holocene to variable but stronger-than-during-the-past-150.000
786 years conditions today, mainly driven by effects of orbital precession.

787

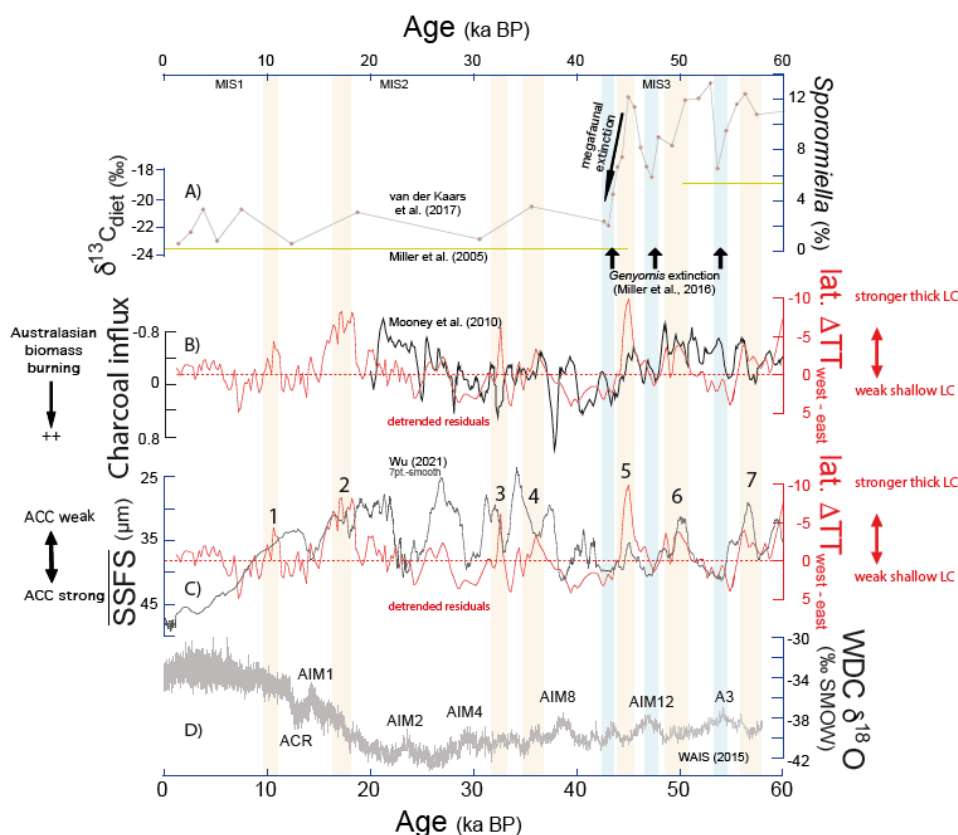
788 **4.4 Australian megafaunal extinction in relation to ocean/climate dynamics**

789 Palynological studies on our western core 2614 record a substantial decline of the dung fungus
790 *Sporormiella*, a proxy for herbivore biomass, which was taken as evidence for the prominent
791 Australian megafaunal population collapse from ~ 45 ka BP to 43.1 ka BP (van der Kaars et al.,
792 2017) (Fig. 8 A). Climate change likely played a significant role in most of the disappearance
793 events of the continent's megafauna during the Pleistocene, while in particular for the last
794 megafaunal population collapse after ~ 45 ka BP human involvement appears possible but is
795 still debated (Wroe et al., 2013).

796 A new chronology constrains the early dispersal of modern humans out of Africa across south
797 Asia into 'Sahul' (North Australia and New Guinea connected by a land bridge at times of
798 glacially lowered sea level; c.f. Saltré et al., 2016) to ~ 65 -50 ka BP (Clarkson et al., 2017;
799 Tobler et al., 2017). The further settlement comprised a single, rapid (within a few thousand
800 years; Tobler et al., 2017) migration along the east and west coasts with Aboriginal Australians
801 reaching the south of Australia by ~ 49 -45 ka BP. It is clear, also, that humans were present in
802 Tasmania by ~ 39 ka BP (Allen and O'Connell, 2014) and in the arid centre of Australia by ~ 35
803 ka BP (Smith, 2013). This places the initial human colonization of Australia clearly before the
804 continent-wide extinction of the megafauna (c.f. Saltré et al., 2016). Rule et al. (2012) and van
805 der Kaars et al. (2017) claimed that human arrival causing overhunting, vegetation change due
806 to landscape burning, or a combination thereof was the primary extinction cause, not climate



807 change. Brook and Johnson (2006) showed with model simulations that species with low
808 population growth rates, such as large-bodied mammals in Australia, might have been easily



809
810 **Figure 8. Variability of Leeuwin Current strength** in comparison to Australian megafaunal extinction, biomass
811 burning, and Antarctic Circumpolar (ACC) strength over the last 60 kyr. A) Record of dung fungus *Sporormiella*
812 percentages in western core 2614, pointing to the Australian megafaunal population collapse at ~45 ka BP to 43.1
813 ka BP (van der Kaars et al., 2017). The yellow lines depict the Australian emu *Dromaius* dietary $\delta^{13}\text{C}$ change
814 documenting a permanent change in food sources (Miller et al., 2005). Three black arrows indicate most probable
815 extinction dates of the Australian megafaunal bird *Genyornis newtoni* at ~54, ~47 and ~43 ka BP (Miller et al.,
816 2016). B) Residuals of detrended lateral (west-east) temperature gradients at thermocline depth reflecting Leeuwin
817 Current strength (red), underlain by the Mooney et al. (2010) record of Australian biomass burning. C) Residuals
818 of detrended lateral (west-east) temperature gradients at thermocline depth reflecting Leeuwin Current strength
819 (red), underlain by the sortable silt record (SSFS; 7pt-smooth) of Drake Passage sediment core PS97-85 reflecting
820 the strength variability of the ACC (Wu et al., 2021). D) West Antarctic Ice Sheet Divide Core $\delta^{18}\text{O}$ record (WAIS
821 Divide Project Members, 2015) as a reference for the southern hemisphere climate signal. Orange shading = short
822 time periods of a strong Leeuwin Current, mostly accompanied by less Australian biomass burning and ACC
823 weakening. Blue shadings = Antarctic warming event (A3) and Antarctic Isotope Maxima (AIM 12, 10). MIS =
824 Marine Isotope Stages 1-3 (Martinson et al., 1987). ACR = Antarctic Cold Reversal.



825 exterminated by even small groups of hunter–gatherers using stone-based tools. Also, Saltré et
826 al. (2016) hypothesized that climate change was not responsible for late Quaternary (last 120
827 kyrs) megafauna extinctions in Australia, as they appeared independent of climate aridity and
828 variability.

829 Our record of detrended $\Delta T T_{\text{west-east}}$, which approximates the strength of the Leeuwin Current,
830 provides additional views on these issues. It shows a robust covariance on millennial to
831 centennial time scales from ~60-20 ka BP to a charcoal composite record reflecting biomass
832 burning in the Australasian region (Mooney et al., 2010) (Fig. 8 B). Commonly, less fires
833 appeared during periods associated with an intensified Leeuwin Current, a southward located
834 STF and Subtropical Ridge, with wetter conditions in the Australasian region at times of a
835 weakened ACC. The consistent timing of changes in both ocean dynamics and biomass burning
836 over such a long period even prior to the arrival of humans in Australia (c.f. Singh et al., 1981)
837 suggests that climate-modulated changes related to the Leeuwin Current led to changes in
838 terrestrial vegetation productivity and distribution, and finally controlled Australasian fire
839 regimes (Mooney et al., 2010). From this point of view, the anthropogenic impact as the main
840 driving mechanism for causing aridification of Australia and for megafaunal extinctions (e.g.
841 Miller et al., 2005) appears unlikely. In the following we argue, however, that it is rather the
842 joint interplay between natural ocean and climate variability, vegetational response, and human
843 interference that caused the Australian megafaunal extinction.

844 Fig. 8 shows the *Sporormiella* record of western core 2614 (van der Kaars et al., 2017) in direct
845 comparison to our detrended record of Leeuwin Current variability. It is evident that before
846 ~45-43.1 ka BP the *Sporormiella* abundances were highly variable, placing *Sporormiella*
847 abundance maxima (>10-13%) into times of extensive thermocline expansion and the strong
848 southward transfer of tropical heat *via* the Leeuwin Current (see above: warming phases 7, 6,
849 5; Fig. 8 A). This is when Antarctica cooled (WAIS Divide Project Members, 2015), and the
850 ACC weakened likely in response to sea ice expansion (Wu et al., 2021) (Fig. 8 C, D).
851 *Sporormiella* minima (<~8%), instead, consistently occurred during times of a shallow
852 thermocline and a weakened Leeuwin Current, with percentages becoming stepwise lower
853 during Antarctic warm periods A3 (~7%) and AIM12 (~6%) until they reach lowest values
854 (~2%) during AIM11 at ~45-43.1 ka BP (Fig. 8 A).

855 The successive decline of *Sporormiella* during Antarctic warm periods and its rapid
856 recuperation in between during times of Antarctic cooling, sea ice expansion, and ACC
857 slowdown is mirrored in the decline of the Australian megafaunal bird *Genyornis newtoni*.



858 From widespread eggshell fragments of *Genyornis* exhibiting diagnostic burn patterns, Miller
859 et al. (2016) concluded that humans depredating and cooking eggs significantly reduced the
860 reproductive success of *Genyornis*. They dated the egg predation and the related extinction of
861 *Genyornis* to ~47 ka BP, although admitting that an age range from ~54 to 43 ka BP could not
862 confidently be excluded (Fig. 8 A). This places the given extinction dates of *Genyornis* into
863 the periods of prominent declines in *Sporormiella* abundances (A3, AIM12, AIM11) and
864 hence, into periods of a weak Leeuwin Current system, while in the warming Southern Ocean
865 (WAIS Divide Project Members, 2015) sea ice extension shrank, and the ACC strengthened
866 (c.f. Wu et al., 2021) (Fig. 8 C).

867 The tight coupling between oceanographic changes and changes in the Australian megafauna
868 as we show brings ocean dynamics as an important player into the game: We hypothesize that
869 the apparent rapid variations in the ocean/climate system from ~60 ka BP to ~43 ka BP with
870 an overall tendency towards a weakening of the Leeuwin Current and the equatorward
871 migration of the Southern hemisphere frontal system (Fig. 8 B) must have caused considerable
872 climatic and ecosystem response in Australia, with negative aftereffects on the continent's
873 megafauna. A recuperation of the megafauna, however, is documented (and expected) by the
874 increasing *Sporormiella* abundances during the short time periods 7, 6, and 5 of an intensified
875 southward transfer of tropical heat *via* the Leeuwin Current and the poleward dislocation of the
876 STR (Fig. 8 B), even though human impact should have persisted or even raised during this
877 period.

878 The final extinction phase defined to ~45-43.1 ka BP on the basis of the core 2614 *Sporormiella*
879 record (van der Kaars et al., 2017) and supported by other studies (e.g. Miller et al., 2005;
880 2016; Rule et al., 2012) appeared synchronous to the significant decline in the core 2614
881 thermocline temperature, salinity, and depth, the reduction of $\Delta T T_{\text{west-east}}$ by more than 10°C,
882 and the clearly warmer and more saline sea surface conditions in the western study area, while
883 the eastern sea surface remained cool and fresh (Figs. 5, 6). This all points to the drastic
884 weakening and shoaling of the Leeuwin Current (analogous to the modern austral summer
885 conditions) with the STF being pushed to the north, and a larger impact of the glacial Southern
886 Ocean *via* an enhanced Flinders Current. The significant re-organization of the ocean
887 circulation south of Australia at ~45-43.1 ka BP is accompanied by a transient change in
888 climate and vegetation in Australia. Bowler et al. (2012) described a drying trend in SE
889 Australia (Willandra Lakes) since ~45 ka, synchronous to the weakening of the Australian
890 monsoon (Johnson et al., 1999) and also visible in the Mooney et al. (2010) charcoal record
891 (Fig. 8 B). The dietary $\delta^{13}\text{C}$ -change of the Australian emu *Dromaius novaehollandiae* at that



892 time (Fig. 8 A) also points to the reorganization of vegetation communities across the
893 Australian semiarid zone (Miller et al., 2005). The abrupt decline in C4-plants between 44 ka
894 BP and 42 ka BP observed in core MD03-2607, however, was interpreted by Lopes dos Santos
895 et al. (2013) not in terms of climate change but in terms of a large ecological change, primarily
896 caused by the absence of the megafaunal browsers due to extinction. The extinction left
897 increased C3-vegetation biomass in the landscape, which would have fostered fires, eventually
898 aided by human activities (Lopes dos Santos et al., 2013).

899 We hypothesize, in contrast, that the centennial-scale severe change in the ocean/climate
900 system beginning at ~45 ka BP must have had aftereffects on the continental environment. We
901 argue that the megafauna, which might have been significantly decimated by human activity
902 at that point, likely did not keep track with the rapidly increasing ecological stress and was no
903 longer able to adopt to the changing conditions related to the weakening of the Leeuwin
904 Current. Humans, in this respect, might indeed have effectively contributed to the extinction
905 of the Australian megafauna as previously suggested (e.g. Rule et al., 2012; Miller et al., 2016;
906 van der Kaars et al.; 2017), but the ocean/climate dynamics provide an important prerequisite
907 and amplifying factor until a tipping point was reached, after which faunal recuperation no
908 longer happened.

909

910 5. Conclusion

911 The Leeuwin Current as important conduit for the poleward heat transport and interocean water
912 exchange between the tropical and the subantarctic ocean areas is highly crucial for the climatic
913 and vegetational evolution of Australia. We note that the western core SST_{Mg/Ca} record broadly
914 follows the modelled El Niño- Southern Oscillation (ENSO) power, relating enhanced SST
915 conditions to strong La Niña conditions in line with high sea level anomalies and strengthened
916 Leeuwin Current volume transport being responsible for the poleward transport of warm
917 waters. The thermocline, instead, reveals changes between the eastward-directed Leeuwin
918 Current System transporting subtropical waters and the westward flow of the Flinders Current
919 System, which brings subantarctic waters into the region.

920 During MIS3, the centennial-scale variations in the Leeuwin Current and the related migrations
921 of the Southern hemisphere frontal system reveal a tendency towards weakening of the
922 Leeuwin Current. It was, instead, strongly developed during Antarctic cool periods at times
923 when the ACC weakened in response to the expanded sea ice cover around Antarctica.

924 During the LGM we note an even narrower, shallower and weaker Leeuwin Current, likely in
925 response to the northward dislocation and shrinking of the Indo-Pacific Warm Pool, which



926 significantly reduced the export of tropical low saline and warm ITW water. The northward
927 shift of the Subtropical Ridge during the LGM likely strengthened the WAC, introducing
928 higher portions of cool SICW into the Leeuwin Current.

929 During deglacial times, the enhanced vertical and lateral temperature gradients point to the
930 rapid formation of a deep thermocline in response to a strengthened Leeuwin Current, and the
931 greater influx of ITW waters at the expense of SICW contributions at times of poleward
932 migration of the STF.

933 During the Holocene, the thermocline off S Australia was considerably shallower compared to
934 the prominent MIS3 and deglacial periods of Leeuwin Current intensification, pointing to a
935 comparably weak Leeuwin Current. After ~6 ka BP, the intensified surface heating near the
936 eastern edge of the Great Australian Bight points to an intensified South Australian Current.
937 At thermocline depth, the strengthened influence of the SABCW and SAMW is visible,
938 transported by an intensified Flinders Current/Leeuwin Undercurrent system.

939 Overall, the Leeuwin Current variability from ~60-20 ka BP captures the biomass burning
940 development in Australasia with less fire when the Leeuwin Current intensified, the STF and
941 the Subtropical Ridge moved southward creating wetter conditions across Australia, and the
942 ACC weakened. The consistent timing of changes suggests that climate-modulated changes
943 related to the Leeuwin Current likely controlled Australasian fire regimes. In consequence we
944 concluded that the concerted action of natural ocean and climate variability, vegetational
945 response, and human interference enhanced the ecological stress on the Australian megafauna
946 until a tipping point was reached at ~43 ka BP, after which faunal recuperation no longer took
947 place.

948

949 **Data availability.** Presented data (Nürnberg et al., 2022a,b) are available online at the Data
950 Publisher for Earth and Environmental Science, PANGAEA (www.pangaea.de):
951 <https://doi.org/.....>; <https://doi.org/.....> (upload currently underway!).

952

953 **Sample availability.** Cores MD03-2614 and MD03-2609 and remaining sample material are
954 stored in the GEOMAR core and rock repository ([https://www.geomar.de/en/centre/central-
955 facilities/tlz/core-rock-repository](https://www.geomar.de/en/centre/central-facilities/tlz/core-rock-repository)).

956

957 **Supplement.** Supporting information associated with this article.

958



959 **Author contributions.** Study conception and design was completed by DN, AK and KM. Data
960 collection was completed by DN, AK, and KM. Data analysis and the interpretation of results
961 was completed by DN, AK, KM and CK. Draft manuscript preparation and editing was
962 completed by DN, AK, KM and CK. All authors reviewed the results and approved the final
963 version of the paper.

964

965 **Competing interests.** The authors declare that they have no conflict of interest.

966

967 **Disclaimer.** Publisher's note: Copernicus Publications remains neutral with regard to
968 jurisdictional claims in published maps and institutional affiliations.

969

970 **Acknowledgements.** We thank the captain, crew, and shipboard scientific crew of R/V
971 MARION DUFRESNE. The studied sediment cores were retrieved during cruise MD131
972 (AUSCAN-campaign) in 2003. We further thank J. Schönfeld as well as lab technicians N.
973 Gehre and S. Fessler for their great support. We are thankful to the reviewers, whose comments
974 considerably helped to improve the manuscript.

975

976 **Financial support.** We thank the German Science Foundation (DFG), which provided initial
977 funding for the recovery of the sediment cores (DFG-project Nu60/11-1).

978

979 **Review statement.** This paper was edited by XXX and re-viewed by XXX and one anonymous
980 referee.

981

982 **References**

983 Allen, J., O'Connell, J.F. (2014). Both half right: updating the evidence for dating first human arrivals in Sahul.
984 *Australian Archaeology*, 79, 86–108.

985 Anand, P., Elderfield, H., Conte, M.H. (2003). Calibration of Mg/Ca thermometry in planktonic foraminifera from
986 a sediment trap time series. *Paleoceanography*, 18 (2).

987 Bahr, A., Nürnberg, D., Karas, C., Grützner, J. (2013). Millennial-scale versus long-term dynamics in the surface
988 and subsurface of the western North Atlantic Subtropical Gyre during marine isotope stage 5. *Global Planetary
989 Change*, 111, 77–87. <https://doi.org/10.1016/j.gloplacha.2013.08.013>.

990 Bahr, A., Hoffmann, J., Schönfeld, J., Schmidt, M.W., Nürnberg, D., Batenburg, S.J., Voigt, S., 2018. Low-
991 latitude expressions of high-latitude forcing during Heinrich Stadial 1 and the Younger Dryas in northern South
992 America. *Global Planetary Change*, 160, 1–9.

993 Barker, S., Greaves, M., Elderfield, H. (2003). A study of cleaning procedures used for foraminiferal Mg/Ca
994 paleothermometry. *Geochemistry, Geophysics, Geosystems*, 4 (9), 8407. doi:10.1029/2003GC000559.



- 995 Barker, P.M. (2004). The circulation and formation of water masses south of Australia and the inter-annual wind
996 variability along the southern Australian coast, PhD. Thesis. University of Melbourne, Victoria, Australia,
997 351pp.
- 998 Barrows, T.T., Juggins, S. (2005). Sea-surface temperatures around the Australian margin and Indian Ocean
999 during the Last Glacial Maximum. *Quaternary Science Reviews*, 24, 1017-1047.
- 1000 Barrows, T.T., Juggins, S., De Deckker, P., Calvo, E., Pelejero, C. (2007). Long-term sea surface temperature and
1001 climate change in the Australian-New Zealand region. *Paleoceanography*, 22 (2), PA2215.
- 1002 Bé, A.W.H., Harrison, S.M., Lott, L. (1973). *Orbulina universa* d'Orbigny in the Indian Ocean.
1003 *Micropaleontology*, 19, 150-192.
- 1004 Bé, A.W.H., Tolderlund, D.S. (1971). Distribution and ecology of living planktonic foraminifera in surface water
1005 of the Atlantic and Indian Oceans. *Micropaleontology of Oceans*, Cambridge University Press, London, 105-
1006 149.
- 1007 Bemis, B.E., Spero, H.J., Bijma, J., Lea, D.W. (1998). Reevaluation of the oxygen isotopic composition of
1008 planktonic foraminifera: Experimental results and revised paleotemperature equations. *Paleoceanography*,
1009 13(2), 150-160.
- 1010 Bostock, H.C., Opydyke, B.N., Gagan, M.K., Kiss, A.E., Fifield, L.K. (2006). Glacial/interglacial changes in the
1011 East Australian current. *Climate Dynamics*, 26, 645–659. doi:10.1007/s00382-005-0103-7.
- 1012 Bowler, J.M., Gillespie, R., Johnston, H., Boljkovac, K. (2012). Wind v water: Glacial maximum records from
1013 the Willandra Lakes. In: S. Haberle, David, B. (eds.) *Peopled landscapes: archaeological and biogeographic*
1014 *approaches to landscapes, Chapter 13, ANU e-press*. doi: 10.22459/TA34.01.2012.13.
- 1015 Boyle, E.A., Keigwin, L.D. (1985/86). Comparison of Atlantic and Pacific paleochemical records for the last
1016 215,000 years: changes in deep ocean circulation and chemical inventories. *Earth Planetary Science Letters*,
1017 76, 135-150.
- 1018 Boyle, E.A., Rosenthal, Y. (1996). Chemical hydrography of the South Atlantic during the Last Glacial
1019 Maximum: Cd vs. $\delta^{13}\text{C}$. In: *Wefer, G., Berger, W.H., Siedler, G., Webb, D. (eds.), The South Atlantic: Present*
1020 *and Past Circulation, Springer, Berlin, Heidelberg*, 423-443.
- 1021 Brook, B.W., Johnson, C.N. (2006). Selective hunting of juveniles as a cause of the imperceptible overkill of the
1022 Australian Pleistocene megafauna. *Alcheringa*, 30, 39–48.
- 1023 Cai, W., van Rensch, P., Cowan, T. (2011). Influence of global-scale variability on the Subtropical Ridge over
1024 Southeast Australia. *Journal of Climate*, 24, 6035-6053. doi: 10.1175/2011JCLI4149.1.
- 1025 Caley, T., Roche, D.M. (2015). Modeling water isotopologues during the last glacial: implications for quantitative
1026 paleosalinity reconstruction. *Paleoceanography*, 30 (6), 739–750.
- 1027 Calvo, E., Pelejero, C., De Deckker, P., Logan, G.A. (2007). Antarctic deglacial pattern in a 30 kyr record of sea
1028 surface temperature offshore South Australia. *Geophysical Research Letters*, 34.
1029 <http://doi.org/10.1029/2007GL029937>.
- 1030 Church, J.A., Cresswell, G.R., Godfrey, J.S. (1989). The Leeuwin Current. Poleward flows along eastern
1031 boundaries. Eds., 34, Coastal and estuarine studies, *American Geophysics Union*, 230-254.
- 1032 Cirano, M., Middleton, J.F., (2004). Aspects of the mean wintertime circulation along Australia's southern
1033 shelves: numerical studies. *Journal of physical oceanography*, 34 (3), 668-684.



- 1034 Clarkson, C., Jacobs, Z., Marwick, B. et al. (2017). Human occupation of northern Australia by 65,000 years ago.
1035 *Nature*, 54(306). doi:10.1038/nature22968.
- 1036 Clement, A.C., Seager, R., Cane, M.A. (1999). Orbital controls on the El Niño/Southern Oscillation and the
1037 tropical climate. *Paleoceanography* 14(4), 441-456.
- 1038 Cléroux, C., Cortijo, E., Duplessy, J.-C. (2008a). Deep-dwelling foraminifera as thermocline temperature
1039 recorders. *Geochemistry, Geophysics, Geosystems*, 8 (4).
- 1040 Cléroux, C., Cortijo, E., Anand, P., Labeyrie, L., Bassinot, F., Caillon, N., Duplessy, J.-C. (2008). Mg/Ca and
1041 Sr/Ca ratios in planktonic foraminifera: Proxies for upper water column temperature reconstruction.
1042 *Paleoceanography*, 23 (3).
- 1043 Courtillot, M., Hallenberger, M., Bassetti, M.-A. et al. (2021). New rRecord of dust input and provenance during
1044 glacial periods in Western Australia shelf (IODP Expedition 356, Site U1461) from the Middle to Late
1045 Pleistocene. *Atmosphere*, 11(11). doi: 10.3390/atmos11111251.
- 1046 Cresswell, G.R., Golding, T.J. (1980). Observations of a southward flowing current in the south-eastern Indian
1047 Ocean. *Deep Sea Research I*, 27 (6), 449-466.
- 1048 Cresswell, G.R., Peterson, J.L. (1993). The Leeuwin Current south of western Australia. *Australian journal of*
1049 *marine and freshwater research*, 44, 285-303.
- 1050 Cresswell, G.R. (2000). Currents of the continental shelf and upper slope of Tasmania. *Papers and Proceedings*
1051 *of the Royal Society of Tasmania*, 133, 21–30.
- 1052 De Deckker, P., Moros, M., Perner, K., Jansen, E. (2012). Influence of the tropics and southern westerlies on
1053 glacial interhemispheric asymmetry. *Nature Geoscience* 5, 266-269.
- 1054 De Deckker, P., van der Kaars, S., Haberle, S., Hua, Q., Stuut, J.-B.W. (2021). The pollen record from marine
1055 core MD03-2607 from offshore Kangaroo Island spanning the last 125 ka; implications for vegetation changes
1056 across the Murray-Darling Basin. *Australian Journal of Earth Sciences*, 68 (7), 928-951. doi:
1057 10.1080/08120099.2021.1896578.
- 1058 Domingues, C.M., Maltrud, M.E., Wijffels, S.E., Church, J.A., Tomczak, M. (2007). Simulated Lagrangian
1059 pathways between the Leeuwin Current System and the upper ocean circulation of the southeast Indian Ocean.
1060 *Deep-Sea Research II*, 54 (8-10), 797-817.
- 1061 Drosowsky, W. (2003). An analysis of Australian seasonal rainfall and teleconnection patterns anomalies: 1950–
1062 1987. II: Temporal variability. *International Journal of Climatology*, 13, 111–149.
- 1063 Drosowsky, W. (2005). The latitude of the subtropical ridge over eastern Australia: The L-index revisited.
1064 *International Journal of Climatology*, 25, 1291-1299.
- 1065 EPICA Community Members (2006). One-to-one coupling of glacial climate variability in Greenland and
1066 Antarctica. *Nature*, 444 (7116), 195-198.
- 1067 Elderfield, H., Vautravers, M., Cooper, M. (2002). The relationship between shell size and Mg/Ca, Sr/Ca, $\delta^{18}\text{O}$,
1068 and $\delta^{13}\text{C}$ of species of planktonic foraminifera. *Geochemistry, Geophysics, Geosystems*, 3(8),
1069 10.1029/2001GC000194.
- 1070 Farmer, E.C., Kaplan, A., de Menocal, P.B., Lynch-Stieglitz, J. (2007). Corroborating ecological depth
1071 preferences of planktonic foraminifera in the tropical Atlantic with stable oxygen isotope ratios of core-top
1072 specimens. *Paleoceanography*, 22, 1-14.



- 1073 Feng, M., Meyers, G., Pearce, A., Wijffels, S. (2003). Annual and interannual variations of the Leeuwin Current
1074 at 32°S. *Journal of Geophysical Research: Oceans*, 108, 33-55.
- 1075 Feng, M., Weller, E. and Hill, K. (2009) The Leeuwin Current. In *A Marine Climate Change Impacts and*
1076 *Adaptation Report Card for Australia 2009* (Eds. E.S. Poloczanska, A.J. Hobday and A.J. Richardson),
1077 NCCARF Publication 05/09, ISBN 978-1-921609-03-9.
- 1078 Findlay, C.S., Flores, J.A. (2000). Subtropical Front fluctuations south of Australia (45°09'S, 146°17'E) for the
1079 last 130 ka years based on calcareous nannoplankton. *Marine Micropaleontology*, 40, 403-416.
- 1080 Fletcher, M.-S., Moreno, P.I. (2011). Zonally symmetric changes in the strength and position of the Southern
1081 Westerlies drove atmospheric CO₂ variations over the past 14 k.y. *Geology*, 39 (5), 419e422.
- 1082 Friedrich, O., Schiebel, R., Wilson, P.A., Weldeab, S., Beer, C.J., Cooper, M.J., Fiebig, J. (2012). Influence of
1083 test size, water depth and ecology on Mg/Ca, Sr/Ca, δ¹⁸O and δ¹³C in nine modern species of planktic
1084 foraminifers. *Earth and Planetary Science Letters*, 319-320, 133-145.
- 1085 Gersonde, R., Crosta, X., Abelmann, A., Armand, L. (2005). Sea-surface temperature and sea ice distribution of
1086 the Southern Ocean at the EPILOG Last Glacial Maximum — a circum-Antarctic view based on siliceous
1087 microfossil records. *Quaternary Science Reviews*, 24, 869–896.
- 1088 Godfrey, J.S., Ridgway, K.R. (1985). The large-scale environment of the poleward-flowing Leeuwin Current,
1089 Western Australia: Longshore steric height patterns, wind stresses and geostrophic flow, *Journal of Physical*
1090 *Oceanography*, 15, 481 – 495.
- 1091 Gottschalk, J., Skinner, L.C., Misra, S., Waelbroeck, C., Menviel, L., Timmermann, A. (2015). Abrupt changes
1092 in the southern extent of North Atlantic Deep Water during Dansgaard–Oeschger events. *Nature Geoscience*, 8,
1093 950. doi: 10.1038/NGEO2558.
- 1094 Grant, K.M., Rohling, E.J., Bar-Matthews, M., Ayalon, A., Medina-Elizalde, M., Ramsey, C.B., Satow, C.,
1095 Roberts, A.P. (2012). Rapid coupling between ice volume and polar temperature over the past 150,000 years.
1096 *Nature* 491 (7426), 744–747.
- 1097 Greaves, M., Caillon, N., Rebaubier, H., Bartoli, G., Bohaty, S., Cacho, I., Clarke, L., Cooper, M., Daunt, C.,
1098 Delaney, M., deMenocal, P., Dutton, A., Eggins, S., Elderfield, H., Garbe-Schönberg, D., Goddard, E., Green,
1099 D., Gröneveld, J., Hastings, D., Hathorne, E., Kimoto, K., Klinkhammer, G., Labeyrie, L., Lea, D.W., Marchitto,
1100 T., Martínez-Botí, M.A., Mortyn, P.G., Ni, Y., Nürnberg, D., Paradis, G., Pena, L., Quinn, T., Rosenthal, Y.,
1101 Russell, A., Sagawa, T., Sosdian, S., Stott, L., Tachikawa, K., Tappa, E., Thunell, R., Wilson, P.A. (2008).
1102 Interlaboratory comparison study of calibration standards for foraminiferal Mg/Ca thermometry. *Geochemistry,*
1103 *Geophysics, Geosystems* 9 (8), Q08010, doi:10.1029/2008GC001974.
- 1104 Hathorne, E.C., Alard, O., James, R.H., Rogers, N.W. (2003). Determination of intratest variability of trace
1105 elements in foraminifera by laser ablation inductively coupled plasma-mass spectrometry. *Geochemistry,*
1106 *Geophysics, Geosystems*, 4(12), 8408, doi:10.1029/2003GC000539.
- 1107 Herzfeld, M., Tomczak, M. (1997). Numerical modelling of sea surface temperature and circulation in the Great
1108 Australian Bight. *Progress in Oceanography*, 39, 29-78.
- 1109 Holbrook, N. J., Davidson, J., Feng, M., Hobday, A.J., Lough, J.M., McGregor, S., Power, S., Risbey, J.S. (2012).
1110 El Niño-southern oscillation. In: *Poloczanska, E.S., Hobday, A.J., Richardson, A.J. (Eds.). A marine climate*
1111 *change impacts and adaptation report card for Australia 2012.*



- 1112 Holbrook, N. J., Goodwin, I. D., McGregor, S., Molina, E., & Power, S. B. (2011). ENSO to multi-decadal time
1113 scale changes in East Australian Current transports and Fort Denison sea level: Oceanic Rossby waves as the
1114 connecting mechanism. *Deep-Sea Research Part I-Topical Studies in Oceanography*, 58(5), 547-558.
1115 doi:10.1016/j.dsr2.2010.06.007
- 1116 Holloway, P.E., Nye, H.C. (1985). Leeuwin Current and wind distributions on the southern part of the Australian
1117 North West Shelf between January 1982 and July 1983. *Australian Journal of Marine and Freshwater Research*,
1118 36, 123-137.
- 1119 Howard, W.R., Prell, W.L. (1992). Late Quaternary surface circulation of the southern Indian Ocean and its
1120 relationship to orbital variations. *Paleoceanography*, 7(1), 79-118. <https://doi.org/10.1029/91PA02994>.
- 1121 Hut, G. (1987). Consultants' group meeting on stable isotope reference samples for geochemical and hydrological
1122 investigations. *International Atomic Energy Agency (IAEA)* (18), 42.
- 1123 James, N.P., Bone, Y. (2011). Neritic carbonate sediments in a temperate realm, Southern Australia. *Springer*,
1124 Berlin254pp.
- 1125 James, N.P., Boreen, T.D., Bone, Y., Feary, D.A. (1994). Holocene carbonate sedimentation on the west Eucla
1126 Shelf, Great Australian Bight: a shaved shelf. *Sedimentary Geology*, 90, 161-177.
- 1127 Johnson, B.J., Miller, G.H., Fogel, M.L., Magee, J.W., Gagan, M.K., Chivas, A.R. (1999). 65,000 years of
1128 vegetation change in central Australia and the Australian Summer Monsoon. *Science*, 284, 1150-1152.
- 1129 Jonkers, L., Kucera, M. (2015). Global analysis of seasonality in the shell flux of extant planktonic foraminifera.
1130 *Biogeosciences*, 12 (7), 2207-2226.
- 1131 Kaiser, J., Lamy, F., Hebbeln, D. (2005). A 70-kyr sea surface temperature record off southern Chile (Ocean
1132 Drilling Program Site 1233). *Paleoceanography*, 20. <http://dx.doi.org/10.1029/2005PA001146>.
- 1133 Karstensen, J., Quadfasel, D. (2002). Formation of Southern Hemisphere Thermocline Waters: Water Mass
1134 Conversion and Subduction. *Journal of Physical Oceanography*, 32, 3020-3038. [https://doi.org/10.1175/1520-0485\(2002\)032<3020:FOSHTW>2.0.CO;2](https://doi.org/10.1175/1520-0485(2002)032<3020:FOSHTW>2.0.CO;2).
- 1136 Kawahata, H. (2002). Shifts in oceanic and atmospheric boundaries in the Tasman Sea (Southwest Pacific) during
1137 the Late Pleistocene: Evidence from organic carbon and lithogenic fluxes. *Palaeogeography Palaeoclimatology
1138 Palaeoecology*, 184(3), 225-249. doi:10.1016/S0031-0182(01)00412-6.
- 1139 Kiernan, K., Fink, D., Greig, D., Mifud, C. (2010). Cosmogenic radionuclide chronology of pre-last glacial cycle
1140 moraines in the Western Arthur range, Southwest Tasmania. *Quaternary Science Reviews* 29(23-24), 3286-
1141 3297.
- 1142 Lamy, F., Arz, H.W., Kilian, R., Lange, C.B., Lembke-Jene, L., Wengler, M., Kaiser, J., Baeza-Urrea, O., Hall,
1143 I.R., Harada, N., Tiedemann, R. (2015). Glacial reduction and millennial-scale variations in Drake Passage
1144 throughflow. *Proceedings of the National Academy of Science USA*, 112, 13496–13501.
- 1145 Legeckis, R., Cresswell, G. (1981). Satellite observations of sea-surface temperature fronts off the coast of western
1146 and southern Australia. *Deep-Sea Research* 28A, 297-306.
- 1147 Li, Q., James, N.P., Bone, Y., McGowan, B. (1999). Paleooceanographic significance of recent foraminiferal
1148 biofacies on the southern shelf of Western Australia: a preliminary study. *Paleoceanography. Paleoclimatology.
1149 Paleoecology* 147, 101-120.
- 1150 Lisiecki, E.L., Raymo, M.E. (2005). A Pliocene-Pleistocene stack of 57 globally distributed benthic $\delta^{18}\text{O}$ records.
1151 *Paleoceanography* 20, PA1003. <https://doi.org/10.1029/2004PA001071>.



- 1152 Locarnini, R.A., Mishonov, A.V., Antonov, J.I., Boyer, T.B., Garcia, H.E., Baranova, O.K., Zweng, M.M., Paver,
1153 C.R., Reagan, J.R., Johnson, D.R., Hamilton, M., Seidkov, D. (2013). Temperature NOAA Atlas NESDIS. *In:*
1154 *Levitus, S. (Ed.), World Ocean Atlas 2013 (1)*.
- 1155 Locarnini, R.A., Mishonov, A.V., Baranova, O.K., Boyer, T.P., Zweng, M.M., Garcia, H.E., Reagan, J.R., Seidov,
1156 D., Weathers, K.W., Paver, C.R., Smolyar, I.V. (2018). Temperature. NOAA Atlas NESDIS. *In: Levitus, S.*
1157 *(Ed.), World Ocean Atlas 2018 (1)*.
- 1158 Lohmann, G.P., Schweitzer, P.N. (1990). *Globorotalia truncatulinoides* ' growth and chemistry as probes of the
1159 past thermocline: 1. Shell size. *Journal of Paleooceanography and Paloclimatology*.
1160 <https://doi.org/10.1029/PA005i001p0005>.
- 1161 Lopes dos Santos, A.R., De Deckker, P., Hopmans, E.C., Magee, J.W., Mets, A., Sinninghe Damsté, J.S.,
1162 Schouten, S. (2013). Abrupt vegetation change after the Late Quaternary megafaunal extinction in south-eastern
1163 Australia. *Nature Geoscience* 6, 627-631.
- 1164 Lopes dos Santos, A.R., Wilkins, D., De Deckker, P., Schouten, S. (2012). Late Quaternary productivity changes
1165 from offshore southern Australia: a biomarker approach. *Paleoceanography. Paleoclimatology. Paleoecology*
1166 363-364, 48-56.
- 1167 Martinez, J.I., De Deckker, P., Barrows, T. (1999). Paleooceanography of the Last glacial maximum in the eastern
1168 Indian Ocean: planktonic foraminifera evidence. *Paleoceanography. Paleoclimatology. Paleoecology*. 147, 73-
1169 99.
- 1170 Martinson, D.G., Pisias, N.G., Hays, J.D., Imbrie, J., Moore, T., Shackleton, N.J. (1987). Age dating and the
1171 orbital theory of the Ice Ages: Development of a high resolution 0 to 30,000-year chronostratigraphy.
1172 *Quaternary Research* 27 (1), 1-29.
- 1173 McBride, J.L. The Australian summer monsoon. *Monsoon Meteorol.* 1987, 203, 13.
- 1174 McCartney, M.S. (1977). Subantarctic Mode Water. *In: Angel, M. (Ed.), A Voyage of Discovery. Supplement to*
1175 *Deep Sea Research* 24, 103-119.
- 1176 McCartney, M.S., Donohue, K.A. (2007). A deep cyclonic gyre in the Australian-Antarctic Basin. *Progress in*
1177 *Oceanography* 75 (4), 675-750.
- 1178 McClatchie, S., Middleton, J., Pattiaratchi, C., Currie, D., Kendrick G. (2006) The south-west marine region:
1179 ecosystems and key species groups. Department of the Environment and Water Resources, ISBN
1180 9780642553815. <https://www.researchgate.net/publication/235223445>.
- 1181 McKenna, V.S., Prell, W.L. (2004). Calibration of the Mg/Ca of *Globorotalia truncatulinoides* (R) for the
1182 reconstruction of marine temperature gradients. *Paleoceanography*, 19 (2).
1183 <https://doi.org/10.1029/2000PA000604>.
- 1184 Meyers, G., Bailey, R.J., Worby, A.P. (1995). Geostrophic transport of Indonesian Throughflow. *Deep-Sea*
1185 *Research*, Part 1, 42, 1163-1174.
- 1186 Michel, E., De Deckker, P., Nürnberg, D. (2003). MD131 / AUSCAN cruise, RV Marion Dufresne.
1187 <https://doi.org/10.17600/3200090>.
- 1188 Middleton, J.F., Cirano, M. (2002). A northern boundary current along Australia's southern shelves: Flinders
1189 Current. *Journal of Geophysical Research: Oceans*, 107 (C9), article 3129.
- 1190 Middleton, J.F., Platov, G. (2003). The mean summertime circulation along Australia's southern shelves: a
1191 numerical study. *Journal of Physical Oceanography*, 33 (11), 2270-2287.



- 1192 Middleton, J.F., Bye, J.A.T. (2007). A review of the shelf-slope circulation along Australia's southern shelves:
1193 Cape Leeuwin to Portland. *Progress in Oceanography* 75 (1), 1-41.
- 1194 Miller, G.H., Fogel, M.L., Magee, J.W., Gagan, M.K., Clarke, S.J., Johnson, B.J. (2005). Ecosystem collapse in
1195 Pleistocene Australia and a human role in megafaunal extinction. *Science*, 309, 287-290. doi:
1196 11.1126/science.1111288.
- 1197 Miller, G., Magee, J., Smith, M. et al. (2016). Human predation contributed to the extinction of the Australian
1198 megafaunal bird *Genyornis newtoni* ~47 ka. *Nature Communication* 7, 10496.
- 1199 Mooney, S.D., Harrison, S.P., Bartlein, P.J. et al. (2010). Late Quaternary fire regimes of Australasia. *Quaternary*
1200 *Science Reviews*. doi:10.1016/j.quascirev.2010.10.010.
- 1201 Moros, M., De Deckker, P., Jansen, E., Perner, K., Telford, R. (2009). Holocene climate variability in the Southern
1202 Ocean recorded in a deep-sea sediment core off South Australia. *Quaternary Science Reviews* 28, 1932-1940.
- 1203 Moss, P.T., Tibby, J., Petherick, L.M., McGowan, H.A., Barr, C. (2013). Late Quaternary vegetation history of
1204 the sub-tropics of Eastern Australia. *Quaternary Science Reviews*, 74, 257-272.
- 1205 Moy, C.M., Seltzer, G.O., Rodbell, D.T., Anderson, D.M. (2002). Variability of El Nino/Southern Oscillation
1206 activity at millennial timescales during the Holocene epoch. *Nature*, 420, 162-165.
- 1207 Newell, B.S. (1961). Hydrology of south-east Australian waters: Bass Strait and New South Wales tuna fishing
1208 area. CSIRO Div. *Fisheries Oceanography Technical Papers*, 10, 22pp.
- 1209 Nürnberg, D., Bijma, J., Hemleben, C. (1996). Assessing the reliability of magnesium in foraminiferal calcite as
1210 a proxy for water mass temperatures. *Geochimica et Cosmochimica Acta*, 60 (5), 803-814.
- 1211 Nürnberg, D., Brughmans, N., Schönfeld, J. (2004). Paleo-export production, terrigenous flux, and sea surface
1212 temperatures around Tasmania – Implications for glacial/interglacial changes in the Subtropical Convergence
1213 Zone. *Geophysical Monograph Series*, 151, 291-318.
- 1214 Nürnberg, D., Groeneveld, J. (2006). Pleistocene variability of the Subtropical Convergence at East Tasman
1215 Plateau: evidence from planktonic foraminiferal Mg/Ca (ODP Site 1172A). *Geochemistry, Geophysics,*
1216 *Geosystems*, 7, Q04P11. [http://dx.doi.org/ 10.1029/2005GC000984](http://dx.doi.org/10.1029/2005GC000984).
- 1217 Nürnberg, D., Ziegler, M., Karas, C., Tiedemann, R., Schmidt, M.W. (2008). Interacting Loop Current variability
1218 and Mississippi River discharge over the past 400 kyr. *Earth and Planetary Science Letters*, 272 (1–2), 278–
1219 289. <https://doi.org/10.1016/j.epsl.2008.04.051>.
- 1220 Nürnberg, D., Bösch, T., Doering, K., Mollier-Vogel, E., Raddatz, J., Schneider, R. (2015). Sea surface and
1221 subsurface circulation dynamics off equatorial Peru during the last ~17 kyr. *Paleoceanography*, 30(7), 984–999.
- 1222 Nürnberg, D., Riff, T., Bahr, A., Karas, C., Meier, K., Lippold, J. (2021). Western boundary current in relation to
1223 Atlantic Subtropical Gyre dynamics during abrupt glacial climate fluctuations. *Global and Planetary Change*,
1224 201. doi: 10.1016/j.gloplacha.2021.103497.
- 1225 Nürnberg, D., et al. (2022a). Geochemical proxy data from sediment core MD03-2614. PANGAEA.
1226 <https://doi.org/>
- 1227 Nürnberg, D., et al. (2022b). Geochemical proxy data from sediment core MD03-2609. PANGAEA.
1228 <https://doi.org/>
- 1229 Paillard, D., Labeyrie, L., Yiou, P. (1996). Macintosh program performs time-series analysis, *Eos Transactions*
1230 *AGU*, 77, 379.



- 1231 Passlow V., Pinxian, W., Chivas, A.R. (1997). Late Quaternary paleocenography near Tasmania, southern
1232 Australia. *Palaeogeography, Palaeoclimatology, Palaeoecology*, 131 433-463.
- 1233 Pattiaratchi, C., Woo, M. (2009). The mean state of the Leeuwin Current system between North West Cape and
1234 Cape Leeuwin. *Journal of the Royal Society of Western Australia* 92, 221-241.
- 1235 Pattiaratchi, C.B., Siji, P. (2020). Variability in ocean currents around Australia. *State and Trends of Australia's*
1236 *Ocean Report*, www.imosoceanreport.org.au. doi: 10.26198/5e16a2ae49e76.
- 1237 Pearce, A.F., Phillips, B.F. (1988). ENSO events, the Leeuwin Current and larval recruitment of the western rock
1238 lobster. *J. Const. Const. Int. Explor. Mer.*, 45, 13-21.
- 1239 Pedro, J.B., van Ommen, T.D., Rasmussen, S.O., Morgan, V.I., Chappellaz, J., Moy, A.D., Masson-Delmotte, V.
1240 (2011). The last deglaciation: Timing the bipolar seesaw. *Climate of the Past*, 7, 671-683.
- 1241 Perner, K., Moros, M., De Deckker, P., Blanz, T., Wacker, L., Telford, R., Siegel, H., Schneider, R., Jansen, E.
1242 (2018). Heat export from the tropic drives mid to late Holocene paleoceanographic changes offshore southern
1243 Australia. *Quaternary Science Reviews*, 180, 96-110.
- 1244 Petherick, L., Bostock, H., Cohen, T.J., Fitzsimmons, K., Tibby, J., Fletcher, M., Fletcher, S., Moss, P., Reeves,
1245 J., Mooney, S., Barrows, T., Kemp, J., Jansen, J., Nanson, G., Dosseto, A. (2013). Climatic records over the
1246 past 30 ka from temperate Australia – a synthesis from the Oz-INTIMATE workgroup. *Quaternary Science*
1247 *Reviews*, 74, 58-77.
- 1248 Regenberg, M., S. Steph, D. Nürnberg, R. Tiedemann, Garbe-Schönberg, D. (2009). Calibrating Mg/Ca ratios of
1249 multiple planktonic foraminiferal species with $\delta^{18}\text{O}$ -calcification temperatures: Paleothermometry for the upper
1250 water column. *Earth and Planetary Science Letters*, 278(3), 324-336.
- 1251 Reißig, S., Nürnberg, D., Bahr, A., Poggemann, D.-W., Hoffmann, J. (2019). Southward displacement of the
1252 North Atlantic subtropical gyre circulation system during North Atlantic cold spells. *Paleoceanography and*
1253 *Paleoclimatology*, 34. <https://doi.org/10.1029/2018PA003376>.
- 1254 Richardson, L.E., Middleton, J.F., Kyser, T.K., James, N.P., Opdyke, B.N. (2018). Water masses and their
1255 seasonal variation on the Lincoln Shelf, South Australia. *Limnology and Oceanography*, 63 (5), 1944-1963.
1256 <https://doi.org/10.1002/lno.10817>.
- 1257 Richardson, L.E., Middleton, J.F., Kyser, T.K., James, N.P., Opdyke, B.N. (2019). Shallow water masses and
1258 their connectivity along the southern Australian continental margin. *Deep-Sea Research, Part 1*,
1259 <https://doi.org/10.1016/j.dsr.2019.103083>.
- 1260 Ridgway, K.R. (2007). Seasonal circulation around Tasmania: an interface between eastern and western boundary
1261 dynamics. *Journal of Geophysical Research*, 112, C10016. <https://doi.org/10.1029/2006JC003898>.
- 1262 Ridgway, K.R., Condie, S.A. (2004). The 5500-km-long boundary flow off western and southern Australia.
1263 *Journal of Geophysical Research: Oceans*, 109 (C4), C04017.
- 1264 Rintoul, S.R., Bullister, J.L. (1999). A late winter hydrographic section from Tasmania to Antarctica. *Deep Sea*
1265 *Research I*, 46, 1417-1454.
- 1266 Rintoul, S.R., Sokolov, S. (2001). Baroclinic transport variability of the Antarctic Circumpolar Current south of
1267 Australia (WOCE repeat section SR3). *Journal of Geophysical Research*, 106 (C2), 2815-2832.
- 1268 Rintoul, S.R., England, M.H. (2002). Ekman transport dominates local air-sea fluxes in driving variability of
1269 Subantarctic Mode Water. *Journal of Physical Oceanography*, 32, 1308-1321.



- 1270 Roberts, J., McCave, I., McClymont, E., Kender, S., Hillenbrand, C.-D., Matano, R., Hodell, D.A., Peck, V.
1271 (2017). Deglacial changes in flow and frontal structure through the Drake Passage. *Earth and Planetary Science*
1272 *Letters*, 474, 397–408.
- 1273 Rochford, J. (1986). Seasonal changes in the distribution of Leeuwin Current waters off southern Australia.
1274 *Australian Journal of Marine and Freshwater Research*, 37, 1-10.
- 1275 Rule, S., Brook, B.W., Haberle, S.G., Turney, C.S.M., Kershaw, A.P., Johnson, C.N. (2012). The aftermath of
1276 megafaunal extinction: Ecosystem transformation in Pleistocene Australia. *Science*, 335, 1483-1486. doi:
1277 10.1126/science.1214261.
- 1278 Saltré, F., Rodríguez-Rey, M., Brook, B.W., et al. (2016). Climate change not to blame for late Quaternary
1279 megafauna extinctions in Australia. *Nature Communications*, 7, 10511. doi: 10.1038/ncomms10511.
- 1280 Schlitzer, R., 2019. Ocean Data View. Available at: <http://odv.awi.de>.
- 1281 Schmidt, G.A., Bigg, G.R., Rohling, E.J. (1999). Global Seawater Oxygen-18 Database - v1.22.
1282 <https://data.giss.nasa.gov/o18data/>.
- 1283 Schmidt, M.W., Lynch-Stieglitz, J. (2011). Florida Straits deglacial temperature and salinity change: Implications
1284 for tropical hydrologic cycle variability during the Younger Dryas. *Paleoceanography*, 26, PA4205.
1285 <https://doi.org/10.1029/2011PA002157>.
- 1286 Schodlok, M.P., Tomczak, M. (1997). The circulation south of Australia derived from an inverse model.
1287 *Geophysical Research Letters*, 24 (22), 2781-2784.
- 1288 Shi, J.-R., Talley, L. D., Xie, S.-P., Liu, W., Gille, S. T. (2020). Effects of buoyancy and wind forcing on Southern
1289 Ocean climate change. *Journal of Climate*. <https://doi.org/10.1175/JCLI-D-19-0877.1>.
- 1290 Singh, G., Kershaw, A.P., Clark, P. (1981). Quaternary vegetation and fire history in Australia. In: Gill, A.M.,
1291 Groves, R.H., Noble, I.R. (Eds.), *Fire in the Australian biota. Australian Academy of Science, Canberra*, 23-54.
- 1292 Smith, M. (2013). *The Archaeology of Australia's Deserts (Cambridge Univ. Press, 2013)*.
- 1293 Smith, R., Huyer, A., Godfrey, S., Church, A.J. (1991). The Leeuwin Current off western Australia, 1986-1987.
1294 *Journal of Physical Oceanography*, 21, 323-345.
- 1295 Speich, S., Blanke, B., de Vries, P., Drijfhout, S., Döös, K., Ganachaud, A., Marsh, R. (2002). Tasman leakage:
1296 a new route in the global ocean conveyor belt. *Geophysical Research Letters*, 29 (10), 1416.
1297 <https://doi.org/10.1029/2001GL014586>.
- 1298 Spooner, M.I., De Deckker, P., Barrows, T.T., Fifield, K.L. (2011). The behaviour of the Leeuwin Current
1299 offshore NW Australia during the last five glacial-interglacial cycles. *Global and Planetary Change*, 75, 119-
1300 132.
- 1301 Sprintall, J., Tomczak, M. (1993). On the formation of central water and thermocline ventilation in the southern
1302 hemisphere. *Deep Sea Research Part I: Oceanographic Research Papers*, 40, 827-848.
1303 [https://doi.org/10.1016/0967-0637\(93\)90074-D](https://doi.org/10.1016/0967-0637(93)90074-D).
- 1304 Suppiah, R. (1992). The Australian summer monsoon: A review. *Progress in Physical Geography*, 16, 283–318.
- 1305 Tedesco, K.A., Thunell, R.C. (2003). Seasonal and interannual variations in planktonic foraminiferal flux and
1306 assemblage composition in the Cariaco Basin, Venezuela. *Journal of Foraminiferal Research*, 33 (3), 192–210.
- 1307 Thompson, R. (1984). Observations of the Leeuwin Current off Western Australia. *Journal of Physical*
1308 *Oceanography*, 14, 623-628.



- 1309 Tobler, R., Rohrlach, A., Soubrier, J. et al. (2017). Aboriginal mitogenomes reveal 50.000 years of regionalism
1310 in Australia. *Nature*. doi:10.1038/nature21416.
- 1311 Toggweiler, J.R., Russell, J.L., Carson, S.R. (2006). Midlatitude westerlies, atmospheric CO₂, and climate change
1312 during the ice ages. *Paleoceanography and Paleoclimatology*. <https://doi.org/10.1029/2005PA001154>.
- 1313 Tudhope, A.W., Chilcott, C.P., McCulloch, M.T. (2001). Variability in the El Niño-Southern Oscillation through
1314 a glacial-interglacial cycle. *Science*, 291, 1511. doi: 10.1126/science.1057969.
- 1315 van der Kaars, S., Miller, G.H., Turney, C.S.M., Cook, J.E., Nürnberg, D., Schönfeld, J., Kershaw, A.P., Lehman,
1316 S.J. (2017). Human rather than climate the primary cause of Pleistocene megafaunal extinction in Australia.
1317 *Nature Communications*, 8, 14142 <https://doi.org/10.1038/ncomms14142>.
- 1318 Vaux, D., Olsen, A.M. (1961). Use of drift bottles in fisheries research. *Aust. Fish. Newsl.* 20, 17-20.
- 1319 WAIS Divide Project Members (2013), Onset of deglacial warming in West Antarctica driven by local orbital
1320 forcing. *Nature*. doi:10.1038/nature12376.
- 1321 Wandres, M. (2018). The influence of atmospheric and ocean circulation variability on the southwest Western
1322 Australian wave climate. *Ph.D. Thesis*, The University of Western Australia.
1323 <https://doi.org/10.4225/23/5ae2a57566b64>.
- 1324 Wells, P.E., Wells, G.M. (1994). Large-scale reorganization of ocean currents offshore Western Australia during
1325 the Late Quaternary. *Marine micropaleontology*, 24, 157-186.
- 1326 Wijeratne, S., Pattiaratchi, C., Proctor, R. (2018). Estimates of surface and subsurface boundary current transport
1327 around Australia. *Journal of Geophysical Research-Oceans*, 123(5), 3444-3466. doi:10.1029/2017jc013221.
- 1328 Wijffels, S., Meyers, G. (2004). An intersection of oceanic waveguides - variability in the Indonesian
1329 Throughflow region. *Journal of Physical Oceanography*, 34, 1232-1253.
- 1330 Williams, A.N., Ulm, S., Cook, A.R., Langley, M.C., Collard, M. (2013). Human refugia in Australia during the
1331 Last Glacial Maximum and terminal Pleistocene: a geospatial analysis of the 25-12 ka Australian archaeological
1332 record. *Journal of Archaeological Science*, 40, 4612-4625.
- 1333 Woo, M., Pattiaratchi, C. (2008). Hydrography and water masses of the western Australian coast. *Deep sea
1334 research I*, 55, 1090-1104.
- 1335 Wroe, S., Field, J.H., Archer, M., et al. (2013). Climate change frames debate over the of megafauna in Sahul
1336 (Pleistocene Australia-New Guinea). *PNAS*, 110(22), 8777-8781. [www.pnas.org/cgi/doi/10.1073/
1337 pnas.1302698110](http://www.pnas.org/cgi/doi/10.1073/pnas.1302698110).
- 1338 Wu, S., Lembke-Jene, L., Lamy, F. et al. (2021). Orbital- and millennial-scale Antarctic Circumpolar Current
1339 variability in Drake Passage over the past 140,000 years. *Nature Communications*. 12:3948.
1340 <https://doi.org/10.1038/s41467-021-24264-9>.
- 1341 Wyrteki, K. (1973). Physical oceanography of the Indian Ocean. In: *Zeitschel, B., Gerlach, S.A., Eds., Ecological
1342 studies: Analysis and Synthesis 3, Springer, Berlin, Heidelberg, 18-36*. [https://doi.org/10.1007/978-3-642-
1343 65468-8_3](https://doi.org/10.1007/978-3-642-65468-8_3).